Research Square

Preprints are preliminary reports that have not undergone peer review.
They should not be considered conclusive, used to inform clinical practice,
or referenced by the media as validated information.

Energy-Level-Matched Electrocatalysis on Au–Nb 2 O 5 /Histidine-Aspartic Acid-Functionalized B,P-Codoped Graphene Quantum Dots for Selective Bisphenol A Detection in infant care products

Li Xinyan
Jiangnan University
Li Ruiyi
ruiyili@jiangnan.edu.cn
Jiangnan University
Li Zaijun
Jiangnan University

Research Article

Keywords: Electrochemical sensing, Bisphenol A, Au–Nb2O5 nanocomposite, Functional graphene quantum dots, Energy-level matching

Posted Date: November 20th, 2026

DOI: https://doi.org/10.21203/rs.3.rs-11604529/v1

License: This work is licensed under a Creative Commons Attribution 4.0 International License.
Read Full License

Additional Declarations: No competing interests reported.

Energy-Level-Matched Electrocatalysis on Au–Nb_2O_5/Histidine-Aspartic Acid-Functionalized B,P-Codoped Graphene Quantum Dots for Selective Bisphenol A Detection in infant care products

Li Xinyan, Li Ruiyi* and Li Zaijun*

School of Life Science and Health Engineering, School of Chemical and Material Engineering, Jiangnan University, Wuxi 214122, China

*Corresponding authors: E-mail address: ruiyili@jiangnan.edu.cn; zaijunli@jiangnan.edu.cn

ABSTRACT

Noble-metal sensing materials are limited by poor selectivity and restricted detection limits in complex-matrix trace analysis, because their zero bandgap enables nonselective electron transfer and precludes energy filtering. To overcome this, an Au–Nb_2O_5 composite decorated with histidine/aspartic acid-functionalized B,P-co-doped graphene quantum dots (HDBP-GQDs) was designed. HDBP-GQD served as chelating agents and interfacial modifiers, sequentially coordinating Nb(V) and Au(III); two-step annealing at 400 and 900 °C then yielded Au–Nb_2O_5/HDBP-GQD composite. Lattice-confined Au atoms formed atomic-scale electron-coupling centers, reducing charge-transfer resistance by >26.7-fold and increasing electroactive surface area by >9.7-fold. Catalytic activity increased by >1.9-fold relative to pristine Nb_2O_5. HDBP-GQD also enabled multi-heteroatom interfacial band engineering, tuning the band gap and interfacial energy levels to match oxidation potential of bisphenol A. This alignment established a selective electron-transfer pathway, in which energy-level gating favored bisphenol A electrooxidation and suppressed coexisting interferents, enhancing catalytic specificity. Among twenty small organic molecules, only bisphenol A elicited a sensitive electrochemical response, confirming excellent selectivity. The sensor exhibited a linear range for bisphenol A of 0.01–150 μM and a detection limit of 0.0031 μM, with reliable performance in infant care products. Beyond bisphenol A sensing, this electronic-state engineering strategy provides a general route to convert zero-bandgap materials into energy-selective electrocatalysts, with broad implications for trace analysis in complex matrices and beyond.

Keywords: Electrochemical sensing; Bisphenol A; Au–Nb_2O_5 nanocomposite; Functional graphene quantum dots; Energy-level matching

1. Introduction

Bisphenol A (BPA) is a key monomer in polycarbonate and epoxy resins, which are widely used in food containers, bottles, and metal-can coatings. Residual BPA can leach into food through hydrolysis and diffusion. This migration is promoted by heat, acidic or fatty conditions, and prolonged storage. Dietary intake is therefore the predominant exposure route [1]. BPA perturbs endocrine signaling through estrogen, androgen, and thyroid receptors and through G protein-coupled estrogen receptor [2]. It also induces oxidative stress, epigenetic changes, and multiple cell-death pathways [3]. These molecular effects have been linked to reproductive, metabolic, cardiovascular, and neurobehavioral disorders. Regulatory assessment is further complicated by low-dose and non-monotonic responses [4]. In response, the European Union has banned BPA in food contact materials and established a 1 μg/kg detection limit, while China is expanding standards to cover multiple matrices [5]. Detection sensitivity and matrix coverage have thus become critical.

Given these regulatory and monitoring demands, analytical methods must balance sensitivity, selectivity, cost, speed, and field applicability. Chromatographic methods remain the conventional mainstay. High-performance liquid chromatography with ultraviolet detection (HPLC-UV) is accessible but insensitive [6]. HPLC with fluorescence detection (HPLC-FD) is more sensitive but inapplicable to non-fluorescent derivatives [7]. Liquid chromatography-tandem mass spectrometry (LC-MS/MS) offers superior qualitative and quantitative performance with ng L^{-1} detection limits, but matrix suppression and high-cost limit routine use [8]. Gas chromatography-mass spectrometry (GC-MS) requires derivatization, which collectively restricts high-frequency monitoring [9]. Immunoassays, such as enzyme-linked immunosorbent assay (ELISA) and immunochromatographic strips, are simple, high-throughput, and inexpensive for screening. However, antibody variability, cross-reactivity, and insufficient strip sensitivity preclude accurate trace quantification [10]. Optical sensors are vulnerable to matrix autofluorescence and color interference [11]. In contrast, electrochemical sensors rely on direct BPA oxidation or recognition-element-mediated electron

transfer. These sensors, using aptamers [12] or molecularly imprinted polymers [13], achieve picomolar to nanomolar detection limits, comparable or superior to chromatographic-mass spectrometric methods. They require only an electrochemical workstation and low-cost disposable electrodes, without derivatization or excessive organic solvents. Miniaturization and smartphone integration enable on-site detection within minutes to tens of minutes, with spike recoveries consistent with LC-MS [14]. Electrochemical sensors therefore best satisfy the trace sensitivity, cost-effectiveness, and on-site operability required for routine BPA monitoring.

Despite these operational advantages, the performance bottleneck in electrochemical BPA determination is governed by the electronic structure and recognition mechanism of sensing materials. Existing electrode-modifying materials include carbon-based conductive materials [15], MXene [16], metal nanomaterials [17], metal-organic frameworks (MOFs) [18], and metal oxide semiconductors [19]. They can provide conductive pathways, enlarge active areas, and enrich analytes. Yet they generally fall into a dilemma of reconciling sensitivity and selectivity. Carbon-based conductive materials, MXene, and metal nanomaterials share zero-bandgap or metallic electronic structures. This feature endows them with high sensitivity but inherently poor selectivity. Their response is essentially a broad-spectrum electrocatalytic oxidation of phenolic hydroxyl groups. It cannot discriminate BPA from coexisting analogues such as bisphenol S and bisphenol F. MOFs possess high surface area and tunable pore architecture, which benefit enrichment. However, they rely predominantly on adsorption-affinity differences. They also suffer from limited aqueous stability, thereby exhibiting adsorption-driven pseudo-selectivity. To overcome the selectivity deficit of zero-bandgap conductive materials, recent attention has turned to metal oxide semiconductors. With bandgaps greater than 3.0 eV, these materials impose a threshold-like energy screening on analyte oxidation potentials. Valence-band electrons must overcome a relatively high energy barrier, thus offering better selectivity than zero-bandgap materials. However, their intrinsic conductivity is insufficient, often necessitating compositing with carbon materials. Moreover, the oxidation-potential difference among bisphenols

is only tens to over one hundred millivolts. This is far below the energy resolution provided by the bandgap, so specificity gains remain limited.

To compensate for the intrinsic selectivity deficiency of these materials, recognition elements have been introduced. These include molecularly imprinted polymers [20], aptamers [21], and enzymes [22]. They are not sensing materials. They provide molecular recognition through complementary shape, size, and functional groups of imprinted cavities, three-dimensional structural matching, or substrate-specific catalysis. Nevertheless, molecularly imprinted polymers are non-conductive and require compositing with conductive materials [23]. Aptamers are relatively costly and susceptible to nuclease degradation. Enzymes are sensitive to temperature and pH with poor reproducibility. Existing strategies therefore remain a compromise between conductivity and selectivity. They do not solve the selectivity problem at the level of electronic structure. Therefore, a new generation of sensing materials is urgently needed: energy-level-matched, energy-selective sensing materials. Their electronic levels are rationally engineered to match the redox potential of the target analyte. This enables target-exclusive electron transfer while suppressing coexisting interferents and matrix background signals. This paradigm shifts the sensing mechanism from adsorption/catalysis-driven broad-spectrum response to energy-level-matched, energy-selective recognition. It offers a fundamental pathway to overcome the intrinsic contradiction between sensitivity and selectivity in electrochemical BPA sensing.

Guided by this principle, we designed an Au–Nb_2O_5 composite decorated with histidine/aspartic acid-functionalized B,P-co-doped graphene quantum dots (HDBP-GQDs). The lattice-confined embedding of Au atoms into Nb_2O_5 lattice creates atomic-level electron-coupling centers. These centers synergistically enhance electrical conductivity and intrinsic catalytic activity. HDBP-GQD further engineers the interfacial band structure, precisely matching the composite's energy levels with the oxidation level of BPA. This matching establishes an energy-gated selective electron-transfer pathway. The pathway drives preferential BPA electrooxidation while suppressing coexisting

interferents. As a result, the Au–Nb_2O_5/HDBP-GQD composite sensor achieves highly sensitive and selective BPA detection in infant care products.

2. Experimental

2.1. HDBP-GQD preparation

Citric acid, histidine, aspartic acid, phosphoric acid, and boric acid were mixed in a molar ratio of 1:1:0.25:0.3:0.3. The mixture was heated at 170 °C for 3 h to give a crude product. This crude product was dissolved in ultrapure water to a concentration of 200 mg mL^{-1} [24]. The solution was filtered to remove large graphitic sheets, dialyzed to remove unreacted precursors, and freeze-dried to obtain solid HDBP-GQD.

2.2. Au–Nb_2O_5/HDBP-GQD synthesis

HDBP-GQD (0.7310 g) was dissolved in deionized water (10 mL). After complete dissolution, aqueous H_2O_2 (10 mL, 30 wt.%) was added slowly. $NbCl_5$ (0.5792 g) was then introduced slowly into the solution. The mixture was stirred for 2 h, after which aqueous ammonia was added dropwise to adjust the pH to about 7. Stirring continued for another 2 h. Subsequently, $HAuCl_4$ solution (7.62 mL, 10 mM) was added, and the mixture was stirred for an additional 2 h. The resulting suspension was transferred to a watch glass containing absorbent cotton and dried in a vacuum oven at 40 °C. The dried precursor was annealed in a tube furnace under N_2 using a two-stage program: heating at 1 °C/min to 400 °C and holding for 1 h, followed by heating at 5 °C min^{-1} to 900 °C and holding for 3 h. This yielded Au–Nb_2O_5/HDBP-GQD. For control samples, Nb_2O_5/HDBP-GQD was prepared identically but without $HAuCl_4$. Nb_2O_5 alone was obtained by calcining Nb_2O_5/HDBP-GQD in air (5 °C/min to 700 °C, held for 3 h).

2.3. Sensor Fabrication

A BPA-sensing film was fabricated on a pre-polished glassy carbon electrode (GCE, 2 mm diameter).

A 7 μL aliquot of Au–Nb_2O_5/HDBP-GQD dispersion (1 mg mL^{-1} in 1.0 wt.% chitosan) was drop-cast onto the GCE surface. High-purity nitrogen was gently blown over the droplet to remove trapped bubbles and promote uniform spreading. The film was then dried completely at a constant temperature. The resulting electrode was stored in a sealed container at 4 °C until use.

2.4. Sample Pretreatment

The collected infant care products were frozen in liquid nitrogen for 15 s and then mechanically broken into small pieces. A known mass of the pieces was placed individually into 40 mL glass bottles with caps, and 10 mL of artificial saliva was added. The artificial saliva was prepared according to a previously reported method [25], and its composition is listed in **Table S1**. After sealing, the bottles were shaken in an orbital shaker at 140 rpm and 37 °C for 30 min. This incubation time was selected based on the potential frequency with which children chew or suck on plastic items. The resulting solution was designated the artificial saliva migration solution (hereafter, migration solution). The migrating compounds were quantified as μg/mL of artificial saliva and μg kg^{-1} of sample, calculated from the exact mass of sample used in each migration experiment.

2.5. Electrochemical Detection of Bisphenol A

BPA working solutions were freshly prepared in 0.1 M PBS (pH 7.4). Each solution was obtained by mixing 1.0 mL of the appropriate BPA stock solution or the artificial saliva migration solution with 5.0 mL of buffer, followed by vortexing at 2000 rpm for 40 s. These mixtures served as the analytes. Electrochemical measurements were performed in a conventional three-electrode cell. The modified GCE served as the working electrode, a KCl-saturated Ag/AgCl electrode as the reference, and a Pt wire as the counter electrode. Cyclic voltammetry (CV) and differential pulse voltammetry (DPV) were recorded over the same potential window to enable direct comparison. For DPV, the step

potential was 50 mV, the pulse width was 60 ms, and the pulse period was 0.5 s. All measurements were conducted at 25 ± 1 °C.

3. Results and discussions

3.1. Design Rationale for Au–Nb_2O_5/HDBP-GQD synthesis

Fig. 1 illustrates the synthetic route to Au–Nb_2O_5/HDBP-GQD. HDBP-GQD was first obtained by one-pot pyrolysis of citric acid, histidine, aspartic acid, boric acid, and phosphoric acid. Citric acid forms the sp^2 carbon framework, while histidine and aspartic acid supply nitrogen, carboxyl, and imidazole coordination sites. Boric and phosphoric acids introduce electron-deficient boron and electron-rich phosphorus, respectively. The pyridine-type nitrogen in histidine imidazole ring is strongly electron-donating and readily coordinates to vacant orbitals of Nb and Au. The aspartic acid side-chain carboxyl groups provide multidentate chelation and hydrogen-bonding sites, enabling uniform metal anchoring at the molecular scale [26]. Phosphorus doping donates electrons and creates defect states, whereas boron doping generates hole-type sites and tunes the Fermi level [27]. This B/P co-doping breaks the electronic symmetry of the graphene quantum dots, strengthens chelation, and modulates semiconductor behavior through impurity levels and charge redistribution. Consequently, HDBP-GQD acts as a reactive platform rather than a passive support, ready for subsequent assembly step.

The synthesis of Au–Nb_2O_5/HDBP-GQD builds on this platform and combines two-step chelation with two-stage thermal annealing. This design temporally separates Au introduction from Au reduction. In the chelation stage, HDBP-GQD first reacts with the Nb source and H_2O_2 under ammonia control to form a Nb–HDBP-GQD complex, pre-organizing the Nb framework. Subsequent addition of Au^{3+} allows it to enter the complex as a coordinated or doped species, rather than being prematurely reduced by HDBP-GQD into free Au nanoparticles. In the annealing stage, the low-temperature step decomposes the precursor and initiates Nb_2O_5 crystallization, while Au species

remain confined within the matrix. The high-temperature step completes Nb_2O_5 crystallization, reduces Au^{3+} in situ to Au^0 dispersed within the lattice, and converts HDBP-GQD into a reduced/carbonized surface layer. This ordered sequence couples Au reduction, oxide crystallization, and GQD surface functionalization. It also prevents the surface segregation and aggregation of Au nanoparticles that often occur in conventional impregnation–reduction methods.

This controlled assembly yields the interface shown at the end of **Fig. 1**. HDBP-GQD anchors to the Nb_2O_5 crystal surface through coordination bonds. Nb–O/N linkages and heteroatom interactions create a strongly coupled interface rather than weak physisorption [28]. The doped energy levels of HDBP-GQD align with the conduction and valence bands of Nb_2O_5, forming a GQD/Nb_2O_5 heterojunction. The interfacial built-in field promotes directional electron transfer. Band realignment narrows the effective bandgap and lowers the charge-transfer barrier. For BPA electrochemical sensing, this architecture provides abundant active sites and improved electron-transport pathways, thereby enhancing the sensing signal.

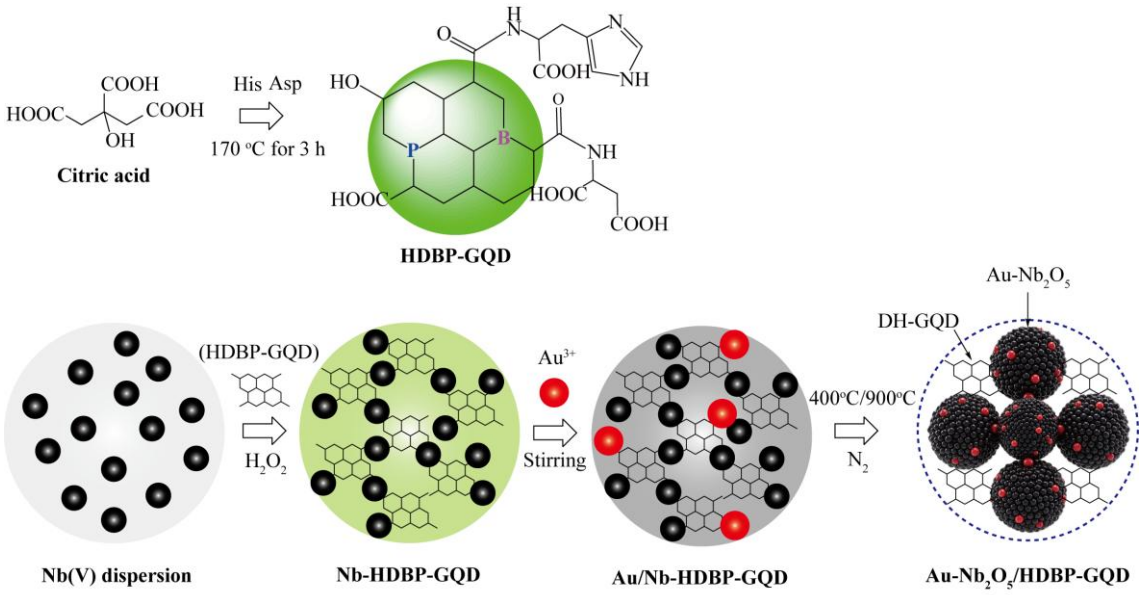


Fig. 1 Synthetic pathway of Au–Nb_2O_5/HDBP-GQD

3.2. Structural Characterization

The SEM and TEM images in **Fig. 2A–C** show that Au–Nb_2O_5/HDBP-GQD adopts a granular/sheet-

like morphology. It consists of interwoven HDBP-GQD sheets and Au–Nb_2O_5 nanodomains. The composite is relatively uniform at the micrometer scale. TEM images show that Au–Nb_2O_5 nanodomains remain highly dispersed within the HDBP-GQD scaffold. Their lateral dimensions are on the nanometer scale, with a relatively narrow size distribution. Magnified TEM images show close contact between Nb_2O_5 nanodomains and HDBP-GQD sheets. Interfacial contrast is continuous, with no evident gaps or phase separation. These morphological and size features may arise from coordination anchoring by B, N, and P heteroatom sites on HDBP-GQD. Such anchoring can suppress migration and aggregation of Au/Nb species during synthesis.

After the overall morphology and size distribution are established, HAADF-STEM in **Fig. 2L** uses Z-contrast to resolve isolated bright spots within Nb_2O_5 nanodomains. Their lateral size is much smaller than nanoparticles resolvable by TEM. It is closer to atomic-scale contrast than to typical Au nanoparticle dimensions. The spots overlap strongly with Nb_2O_5 nanodomains. This suggests atomic-level dispersion of heavy-element species, such as Au. HAADF intensity depends on both atomic number and sample thickness. Isolated bright spots alone cannot serve as the sole criterion for Au atoms [29]. Their size and spatial overlap nevertheless provide important evidence for atomic-level coexistence of Au with Nb_2O_5.

Linked to the morphology and atomic dispersion results, HRTEM, SAED, IFFT, and intensity profiles in **Fig. 2D–G** reveal crystallographic features and crystallite size. The clear lattice fringes in HRTEM mainly correspond to characteristic Nb_2O_5 facets. Their limited extension suggests small Nb_2O_5 crystallites. This is consistent with the polycrystalline rings in the SAED pattern. HRTEM shows no Au(111), Au(200), or other typical Au lattice fringes. SAED in **Fig. 2E** also lacks diffraction signals from independent Au crystals. This negative evidence indicates that no diffraction-detectable independent Au crystals are present in the selected region. It places crystallographic constraints on Au existing as highly dispersed, atomic, or ionic species within Nb_2O_5 domains.

On this crystallographic basis, IFFT and intensity profiles further reveal local periodicity changes

in the Nb_2O_5 lattice. IFFT reconstruction shows continuous lattice fringes overall. Local contrast anomalies and period perturbations are still visible. Intensity profiles show local fluctuations and distortions in interplanar spacing. These lattice distortions may arise from heteroatom occupancy, oxygen vacancy formation, charge compensation, or local strain relaxation. They are consistent with Au incorporation into the Nb_2O_5 lattice perturbing the original periodic potential. Combined with the finite domain size in HRTEM and polycrystalline rings in SAED, a relatively high density of local defects or distorted regions inside the Nb_2O_5 lattice can be inferred. However, IFFT and intensity profiles are not element-specific. Lattice distortions can also arise from thickness variation, defocus, defects, or other dopants. They must therefore be interpreted together with elemental mapping and valence analysis.

Building on lattice distortion analysis, atomic strain distributions in **Fig. 2H–K** move structural characterization toward local strain engineering. Strain tensor analysis along Exx and Eyy shows pronounced anisotropic local strain in Au–Nb_2O_5 regions. Tensile and compressive domains alternate. If Au were only surface-loaded, strain would be confined mainly to the surface or interface. Here, strain extends into the Nb_2O_5 lattice. This is more consistent with heteroatom occupancy, lattice mismatch, or defect-induced long-range/local lattice relaxation [30]. Such strain fields can tune the Nb_2O_5 d-band center, oxygen vacancy formation energy, and interfacial charge-transfer barrier. They can thereby affect the electronic structure of active sites. Strain analysis alone cannot identify the occupying element. It must be cross-checked with Au elemental distribution and valence information. Elemental mapping in **Fig. 2M–S** provides the spatial distribution of Au from a compositional perspective. C, B, N, and P signals mainly come from the HDBP-GQD scaffold. This indicates relatively uniform heteroatom doping in the carbon matrix. O and Nb signals co-localize in Nb_2O_5 nanodomains. The Au signal does not form independent enrichment domains. Its spatial extent matches the Nb and O domains and strongly overlaps with them. This compositional feature constrains Au to atomic-level dispersion within Nb_2O_5 domains, rather than independent Au crystals

or nanoparticles. B, N, and P heteroatoms can enhance the donor–acceptor character of HDBP-GQD. They may also coordinate and stabilize Au species. This suppresses migration and aggregation during synthesis and under operating conditions.

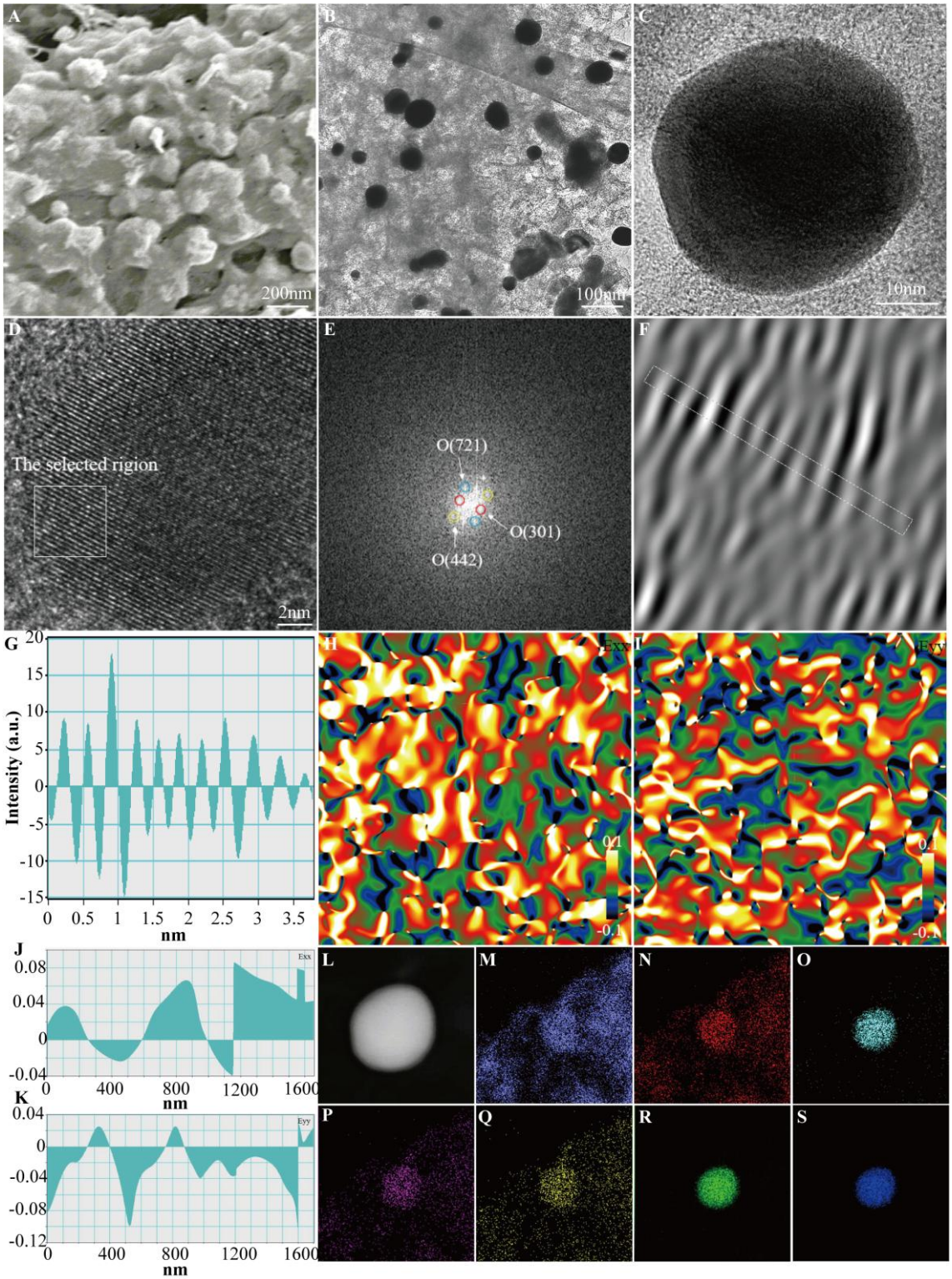


Fig. 2 SEM (A), TEM (B), enlarged TEM (C), and HRTEM images (D) of Au–Nb_2O_5/HDBP-GQD, SAED pattern (E), IFFT pattern (F), intensity profile (G) and atomic strain distributions in E_{xx} and E_{yy} directions (H, I, J, and K), HAADF-STEM image (L), and elemental mappings of C (M), B (N), P (O), N (P), O (Q), Nb (R), and Au elements (S)

The XRD pattern of Au-Nb_2O_5/HDBP-GQD is shown in **Fig. 3A**. The sample exhibits sharp diffraction peaks from 23.59° to 88.12° with a flat baseline and no obvious amorphous halo. This indicates high crystallinity and long-range order for Nb_2O_5 component. All major peaks match PDF#72-1484 and are indexed to monoclinic H-Nb_2O_5. The peaks at 23.59°, 25.36°, 26.65°, 32.24°, 36.58°, 39.74°, 41.85°, 44.23°, 47.41°, 54.13°, 58.82°, 60.47°, 64.82°, 66.96°, 72.70°, 77.83°, and 88.12° correspond to the (101), (530), (301), (114), (541), (721), (930), (860), (002), (442), (724), (1011), (820), (519), (1311), (1227), and (738) planes, respectively. No impurity peaks are observed, confirming a pure monoclinic H phase. According to PDF#72-1484, this phase has space group P2/m (No. 10) with a = 21.153 Å, b = 3.823 Å, c = 19.356 Å, and β = 119.8°. The space group and the projection along the c-axis (**Fig. 3B**) show that NbO_6 octahedra connect by corner- and edge-sharing to form a Wadsley-Roth shear structure. This structure creates open tunnels along the b-axis. These tunnels provide fast diffusion pathways for electrolyte ions. In PBS (pH 7.4), the main mobile ions are Na^+ and K^+. Such ion transport is beneficial for the electrochemical sensing of BPA. No face-centered cubic Au peaks (38.1°, 44.3°, 64.5°) are observed. This agrees with Au being atomically dispersed as single atoms, which do not form long-range ordered crystals and give no detectable XRD signal. HDBP-GQD is amorphous or nanocrystalline, and its diffuse scattering is indistinguishable from the sharp Nb_2O_5 peaks. Thus, neither Au nor HDBP-GQD forms separate crystalline phases, and neither disrupts the Nb_2O_5 framework.

To further verify the phase assignment and obtain quantitative structural parameters, we performed Rietveld refinement using the monoclinic H-Nb_2O_5 (P2/m) model from PDF#72-1484 as the starting

point. The refinement was carried out in GSAS/EXPGUI. Peak shapes were described by a pseudo-Voigt function. Background was fitted with a shifted Chebyshev polynomial to account for diffuse scattering from amorphous HDBP-GQD. We sequentially refined the scale factor, zero shift, background coefficients, lattice parameters, peak shape parameters, and atomic temperature factors. Because Au is atomically dispersed at low loading, its scattering contribution is negligible and was not included as a separate phase. The refinement converged well with R_{wp} = 8.2%, R_p = 6.5%, and GOF = 1.35, indicating a reliable structural model. The refined lattice parameters are a = 21.15(1) Å, b = 3.825(3) Å, c = 19.36(1) Å, and β = 119.8(2)°, which match the standard values from PDF#72-1484. The average Nb—O bond length is about 1.98 Å, and the average bond angle deviation of NbO_6 octahedra is about 5.8°. This reflects significant octahedral distortion due to the low symmetry of P2/m. The residual curve is flat across the entire 2θ range with no systematic deviations, confirming that the monoclinic P2/m model explains the main diffraction features. Using the peak shape parameters, we estimated microstructural parameters by the Williamson-Hall method. The average crystallite size of Nb_2O_5 is about 18.6 nm, and the microstrain is about 0.32%. This moderate microstrain may arise from interactions between Au single atoms and the Nb_2O_5 support, as well as lattice perturbations from HDBP-GQD surface modification. In summary, XRD analysis and Rietveld refinement show that Nb_2O_5 in Au-Nb_2O_5/HDBP-GQD is monoclinic H phase (space group P2/m, No. 10), matching PDF#72-1484 well. It has good crystallinity and high phase purity. The space group and crystal structure projection both reveal open tunnels along the b-axis, which facilitate electrolyte ion transport in PBS. Au exists as atomically dispersed single atoms, and HDBP-GQD is amorphous. Neither form separate crystalline phases, and neither significantly affects Nb_2O_5 crystal framework.

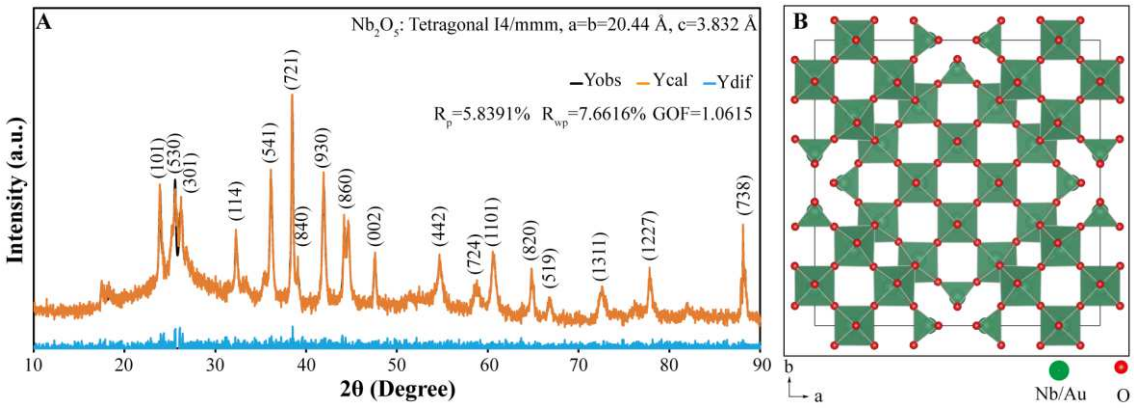


Fig. 3 XRD pattern of Au-Nb_2O_5/HDBP-GQD, with peaks indexed to monoclinic H-Nb_2O_5 (PDF#72-1484) (A), and crystal structure projection along the c-axis, showing the P2/m symmetry and open tunnels along the b-axis (B)

The FTIR spectrum of Au-Nb_2O_5/HDBP-GQD (**Fig. 4A**) shows a broad and strong band near 3424.19 cm^{-1} from O—H/N—H stretching. This indicates abundant hydroxyl and amino groups, as well as adsorbed water, on the surface and at defect sites [31]. Weak bands at about 2897.47 cm^{-1} arise from symmetric and asymmetric C—H stretching of sp^3 carbon. The absorption band at 1538.92 cm^{-1} region contains C=C skeletal vibrations of the HDBP-GQD network and C=O stretching. Thus, graphitic sp^2 domains coexist with oxygen-containing groups. Between 1200 and 1450 cm^{-1}, overlapping C—N, C—O, B—O, and P=O/P—O vibrations appear. These features confirm that N, B, and P heteroatoms and phosphate groups are incorporated into the carbon framework or exist as surface ligands. Nb—O—Nb and Nb—O vibrations at 500–900 cm^{-1} show that the Nb_2O_5 framework is retained. Several P=O, P—O, and Nb—O bands shift relative to single Nb_2O_5 or HDBP-GQD. This shift points to coordination or hydrogen bonding between HDBP-GQD functional groups and Nb_2O_5 surfaces. Such interfacial contact can limit Nb_2O_5 aggregation and provide anchoring sites for Au. The XPS survey spectrum (**Fig. 4B**) shows C, N, O, P, B, Nb, and Au signals. This result agrees with FTIR and confirms that all target elements are present. Strong C and O signals indicate that GQD and oxygen-containing groups dominate the surface. N, P, and B signals verify multi-heteroatom doping. Nb and Au signals confirm successful loading of Nb_2O_5 and Au species.

High-resolution XPS gives further information on chemical states and interfacial electron coupling.

The C1s spectrum is fitted to four components at 284.8, 285.87, 286.84, and 288.77 eV, assigned to C—C/C=C, C—N, C—O, and O=C—O (**Fig. 4C**). These groups show that N and O are incorporated into the carbon skeleton or bonded at edges [32]. They can also anchor Nb and Au sites. The N1s spectrum contains pyridinic N at 398.71 eV and pyrrolic N at 401.08 eV (**Fig. 4D**). Pyridinic N can donate its lone pair to vacant Nb or Au orbitals. Pyrrolic N helps tune the carbon electronic structure and improve conductivity. The O1s spectrum is resolved into lattice oxygen ($O_{lat.}$) at 530.78 eV, adsorbed oxygen ($O_{ads.}$) at 531.76 eV, and surface hydroxyl/water (O_w) at 533.19 eV (**Fig. 4E**). $O_{ads.}$ is linked to oxygen vacancies, low-coordinate oxygen, and surface defects. This assignment is consistent with the mixed Nb valence states. The P2p spectrum has P—C/P—N at 134.15 eV and P—O/P=O at 130.86 eV (**Fig. 4F**). P is thus incorporated into the carbon framework and remains in HDBP-GQD phosphate groups. P can adjust local charge distribution and coordinate with Nb sites on Nb_2O_5.The B1s spectrum shows BC_3 at 189.68 eV, BC_2O at 191.25 eV, and BCO_2 at 192.21 eV (**Fig. 4G**). Therefore substitutes graphitic carbon and also participates in oxygen-containing edge structures. This doping can create hole-type features, strengthen O_2 adsorption, and promote interfacial charge transfer. The Nb3d spectrum shows Nb^{4+} $3d_{5/2}$ at 206.52 eV, Nb^{5+} $3d_{5/2}$ at 207.79 eV, Nb^{4+} $3d_{3/2}$ at 209.09 eV, and Nb^{5+} $3d_{3/2}$ at 210.53 eV, with a spin-orbit splitting of about 2.7 eV (**Fig. 4H**). Nb^{5+} remains the main state in Nb_2O_5, while partial Nb reduction creates Nb^{4+} and oxygen vacancies. The Nb^{4+}/Nb^{5+} pair can improve electron transport and form a defect-rich surface [33]. The Au4f spectrum shows Au^0 $4f_{7/2}$ at 84.24 eV, Au^+ at 85.09 eV, Au^0 $4f_{5/2}$ at 87.91 eV, and Au^+ at 88.90 eV, with a spin-orbit splitting of 3.67 eV (**Fig. 4I**). The coexistence of Au^0 and Au^+ indicates highly dispersed Au and interfacial electron transfer with HDBP-GQD and Nb_2O_5 [34]. Together, FTIR and XPS show that Au-Nb_2O_5/HDBP-GQD is not a simple physical mixture. C—N, C—O, O=C—O, P=O/P—O, and B—O groups anchor the components. Nb^{4+}/Nb^{5+} and Au^0/Au^+ redox pairs, together with Oads.-related oxygen vacancies, create a strongly coupled multi-level interface. This interface offers abundant active sites, fast electron pathways, and stable anchoring. These features are desirable

for catalysis, sensing, and electrochemical applications.

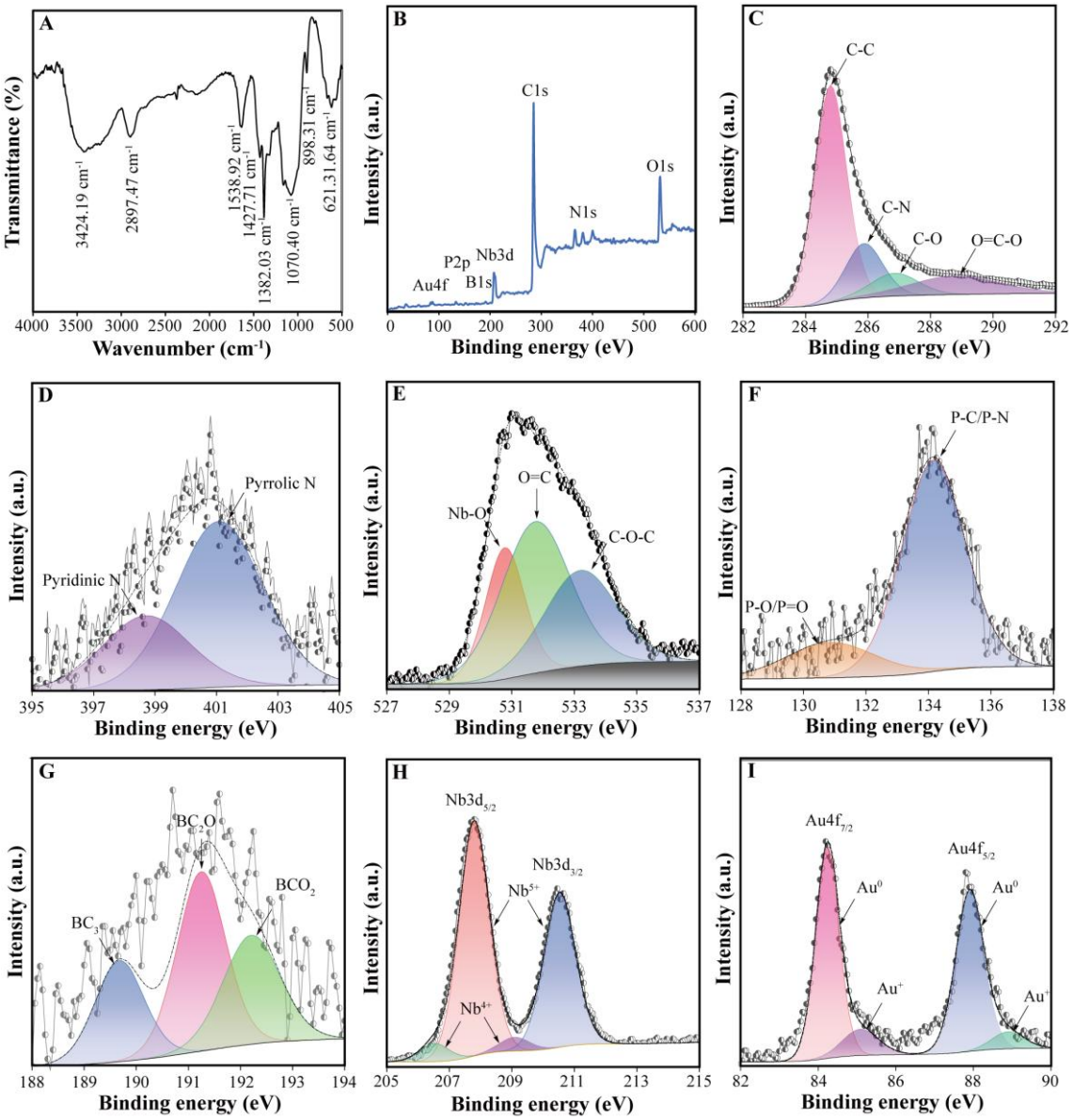


Fig. 4 FTIR spectrum (A), total XPS spectrum of Au-Nb_2O_5/HDBP-GQD (B), and high-resolution XPS spectra of C1s (C), N1s (D), O1s (E), P2p (F), B1s (G), Nb2p (H), and Au4f (I)

The structural data converge on a clear picture. B/N/P-doped HDBP-GQD acts as the anchoring scaffold. Monoclinic H-Nb_2O_5 provides the crystalline host. Au is atomically dispersed. It forms no separate crystals or nanoscale domains. Au overlaps the Nb/O regions and disturbs the local lattice. This disturbance produces microstrain, lattice distortion, and oxygen vacancies. The Nb_2O_5 framework remains crystalline and keeps its b-axis tunnels. FTIR and XPS identify C-N, C-O, P=O/P-

O, and B-O interfacial linkages. They also reveal Nb^{4+}/Nb^{5+}, Au^0/Au^+, and $O_{ads.}$-related defects. These coupled features support stable anchoring, fast ion/electron transport, and abundant active sites. The resulting interface is promising for catalysis and electrochemical sensing.

3.3. Electrocatalytic Behavior of Au–Nb_2O_5/HDBP-GQD

The electrocatalytic response of Au–Nb_2O_5/HDBP-GQD was benchmarked against bare GCE, Nb_2O_5/GCE, and Nb_2O_5/HDBP-GQD/GCE. The CV curves were acquired in 1 mM $K_4Fe(CN)_6$ in the PBS of pH 7.4 at scan rate of 10 mV s^{-1} (**Fig. 5A**). All modified electrodes delivered higher redox currents than bare GCE, confirming that Nb_2O_5, Nb_2O_5/HDBP-GQD, and Au–Nb_2O_5/HDBP-GQD facilitate the $Fe(CN)_6^{3-/4-}$ redox process. The response increased in the order Nb_2O_5 < Nb_2O_5/HDBP-GQD < Au–Nb_2O_5/HDBP-GQD. The composite therefore provided the most active interface. For quantitative comparison, ΔI_p between the anodic and cathodic peaks was extracted from **Fig. 5A** and plotted in **Fig. 5B**. The values were 57.51, 77.053, and 102.726 μA for Nb_2O_5, Nb_2O_5/HDBP-GQD, and Au–Nb_2O_5/HDBP-GQD, respectively. Relative to Nb_2O_5, the latter two electrodes showed 1.34-fold and 1.79-fold enhancements. These non-additive gains point to a synergistic effect rather than a simple combination of components.

The enhanced activity is rooted in the composite architecture. The B/N/P-doped HDBP-GQD acts as an anchoring scaffold, while monoclinic H-Nb_2O_5 provides a crystalline host with b-axis tunnels. Atomic Au remains dispersed, without forming separate crystals or nanodomains. It overlaps Nb/O domains and locally perturbs the lattice, generating microstrain, lattice distortion, and oxygen vacancies. Interfacial C–N, C–O, P=O/P–O, and B–O linkages form at the heterojunction. Together with Nb^{4+}/Nb^{5+}, Au^0/Au^+, and $O_{ads.}$-related defects, these features stabilize the interface, accelerate ion/electron transport, and supply abundant active sites. This structural coupling accounts for the improved $Fe(CN)_6^{3-/4-}$ kinetics and the largest ΔI_p observed for Au–Nb_2O_5/HDBP-GQD.

To probe the origin of this improvement, EIS and scan-rate-dependent CV were performed in 1.0

M Na_2SO_4. These measurements yielded the charge-transfer resistance (R_{ct}) and the ECSA-related capacitive parameter k [35] (**Fig. 5C–F**). The Nyquist plots in **Fig. 5C** gave fitted R_{ct} values of approximately 581.3, 375.1, and 21.77 Ω for Nb_2O_5, Nb_2O_5/HDBP-GQD, and Au–Nb_2O_5/HDBP-GQD, respectively (**Fig. 5D**, **Table S2**). The R_{ct} of Au–Nb_2O_5/HDBP-GQD was about 26.7-fold lower than that of Nb_2O_5 and 17.2-fold lower than that of Nb_2O_5/HDBP-GQD. This drop reflects substantially faster interfacial charge transfer. In contrast, k values obtained from the ΔJ–v plots (**Fig. 5E,F** and **Fig. S1**) were 0.0547, 0.4103, and 0.5329 for Nb_2O_5, Nb_2O_5/HDBP-GQD, and Au–Nb_2O_5/HDBP-GQD, respectively. Because k scales with double-layer capacitance and thus with ECSA, the upward trend indicates that Au–Nb_2O_5/HDBP-GQD has the largest ECSA. The highest electrocatalytic activity therefore arises from the lowest R_{ct} and the largest ECSA (>9.7-fold that of Nb_2O_5).

Collectively, the structural and electrochemical data show that the activity of Au–Nb_2O_5/HDBP-GQD is governed by two coupled factors: a low charge-transfer barrier and a large accessible electroactive area. Dispersed atomic Au, interfacial linkages, and defect states lower R_{ct}, while the HDBP-GQD/Nb_2O_5 architecture enlarges ECSA. This combination, rather than any single component, accounts for the superior $Fe(CN)_6^{3-/4-}$ response.

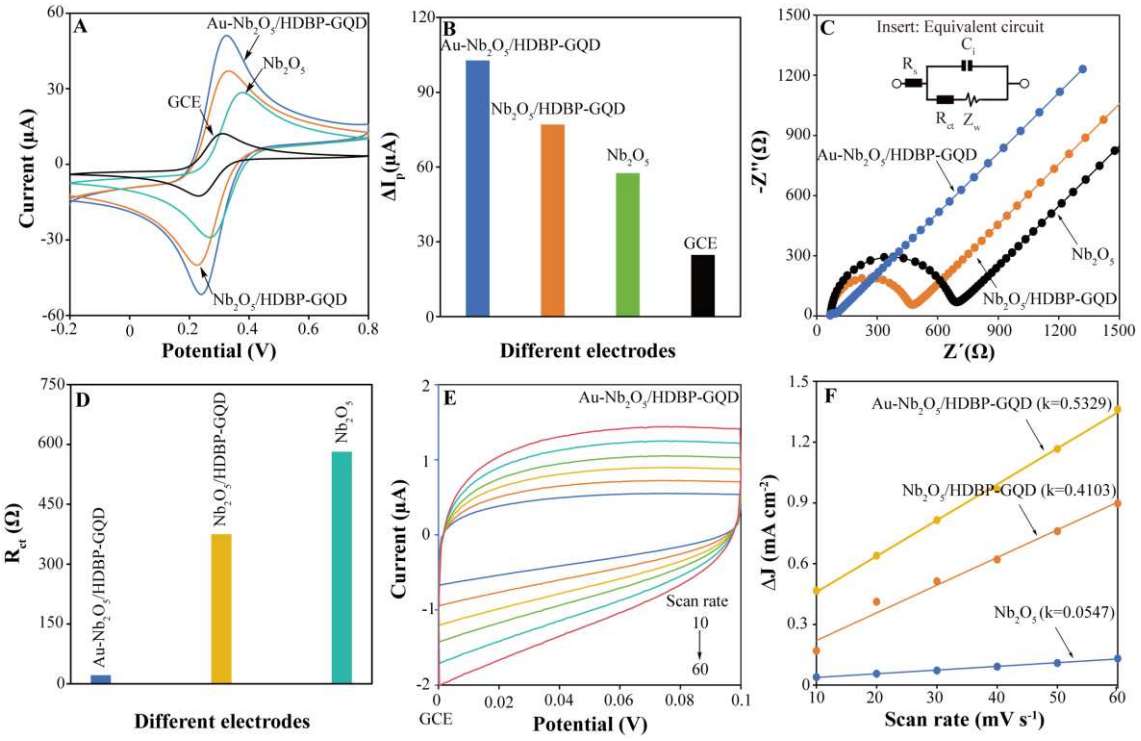


Fig. 5 CV curves (A) of the bare GCE and GCEs modified with Nb_2O_5, Nb_2O_5/HDBP-GQD and Au-Nb_2O_5/HDBP-GQD in 1 mM $K_4Fe(CN)_6$ (PBS, pH 7.4) at 10 mV s^{-1} and corresponding ΔI_p values (B), Nyquist plots of Nb_2O_5, Nb_2O_5/HDBP-GQD and Au-Nb_2O_5/HDBP-GQD electrodes in 1.0 M Na_2SO_4 aqueous electrolyte (C) and corresponding R_{ct} values (D), and the CV curves of Au-Nb_2O_5/HDBP-GQD electrodes (E) in 1 mM $K_4Fe(CN)_6$ (PBS, pH 7.4) at 10–60 mV s^{-1} and plots of Plots of the ΔJ versus scan rate for the Nb_2O_5, Nb_2O_5/HDBP-GQD and Au-Nb_2O_5/HDBP-GQD electrodes

To evaluate the electrocatalytic selectivity of Au–Nb_2O_5/HDBP-GQD, twenty small organic molecules commonly present in biological samples were probed by CV in PBS (pH 7.4) over a potential window of −0.2 to 0.8 V at 10 mV s^{-1}. A central issue was to distinguish Faradaic catalysis from capacitive charging. The responses in **Fig. 6** fall into three categories, providing a framework for mechanistic interpretation.

Category I is defined by weak currents and unresolved redox peaks. It includes alanine, tyrosine, dopamine, serine, arginine, tryptophan, and histidine. Alanine, serine, and arginine lack oxidizable motifs. Tyrosine, tryptophan, and histidine contain phenol, indole, or imidazole groups, yet their

oxidation potentials lie outside the applied window. At pH 7.4, their charge states further disfavor accumulation at the negatively charged surface. Dopamine behaves differently. Its catecholamine moiety can coordinate to Au sites, and its oxidation product can form an insulating polydopamine film that blocks subsequent electron transfer. In addition, at 1 μM the Faradaic signal is too small to be distinguished from the background.

Category II exhibits strong currents without a well-defined redox peak pair. It comprises ascorbic acid, acetaminophen, glutamic acid, uric acid, levodopa, hydroquinone, glutathione, catechol, glucose, cysteine, glycine, and urea. Several of these analytes are anionic at pH 7.4—ascorbic acid, uric acid, glutamic acid, cysteine, and glutathione—and are electrostatically repelled by the negative electrode. Ascorbic acid and uric acid undergo irreversible oxidation, so no reduction peak appears. Cysteine and glutathione coordinate Au through thiol groups and block catalytic sites. Acetaminophen, levodopa, hydroquinone, and catechol possess phenolic hydroxyls, but their oxidation products are water-soluble or adopt poor adsorption orientations. Their peaks broaden and merge with capacitive charging. Glucose, urea, and glycine lack oxidizable groups. Their currents arise mainly from the high ECSA, defect sites, and surface functionalities of HDBP-GQD and Nb_2O_5. Thus, a strong current alone does not indicate selective catalysis.

Category III is characterized by a strong current and a distinct oxidation peak. Bisphenol A is its only member. BPA contains two para-phenolic hydroxyls and a hydrophobic aromatic core, with a pK_a of approximately 9.6–10.2. At pH 7.4, it is predominantly neutral and is not repelled by the negative surface. Its aromatic rings can accumulate on sp^2 carbon domains and doped sites of HDBP-GQD through π–π stacking and hydrophobic interactions. This enrichment increases the local concentration above that in bulk solution. At Au sites, the phenolic hydroxyls are oxidized. The Nb^{4+}/Nb^{5+} couple and oxygen vacancies promote proton-coupled electron transfer. $O_{ads.}$ and interfacial C–O, B–O, and P=O linkages stabilize the quinone-type intermediate and lower the overpotential. As a result, BPA gives the only clear oxidation peak despite the high capacitive

background. Its reduction peak remains weak, indicating irreversible oxidation. The response therefore reflects a coupled enrichment–catalysis–electron transfer process.

Together, these categories show that Au–Nb_2O_5/HDBP-GQD does not act as a broad-spectrum electrocatalyst. Its selectivity depends on the match between analyte properties—pK_a, charge, hydrophobicity, coordination ability, and oxidation reversibility—and the interfacial microenvironment. Only BPA satisfies this match. The electrode therefore provides excellent selectivity for BPA oxidation. It is a promising selective electrochemical recognition interface for BPA in complex biological matrices.

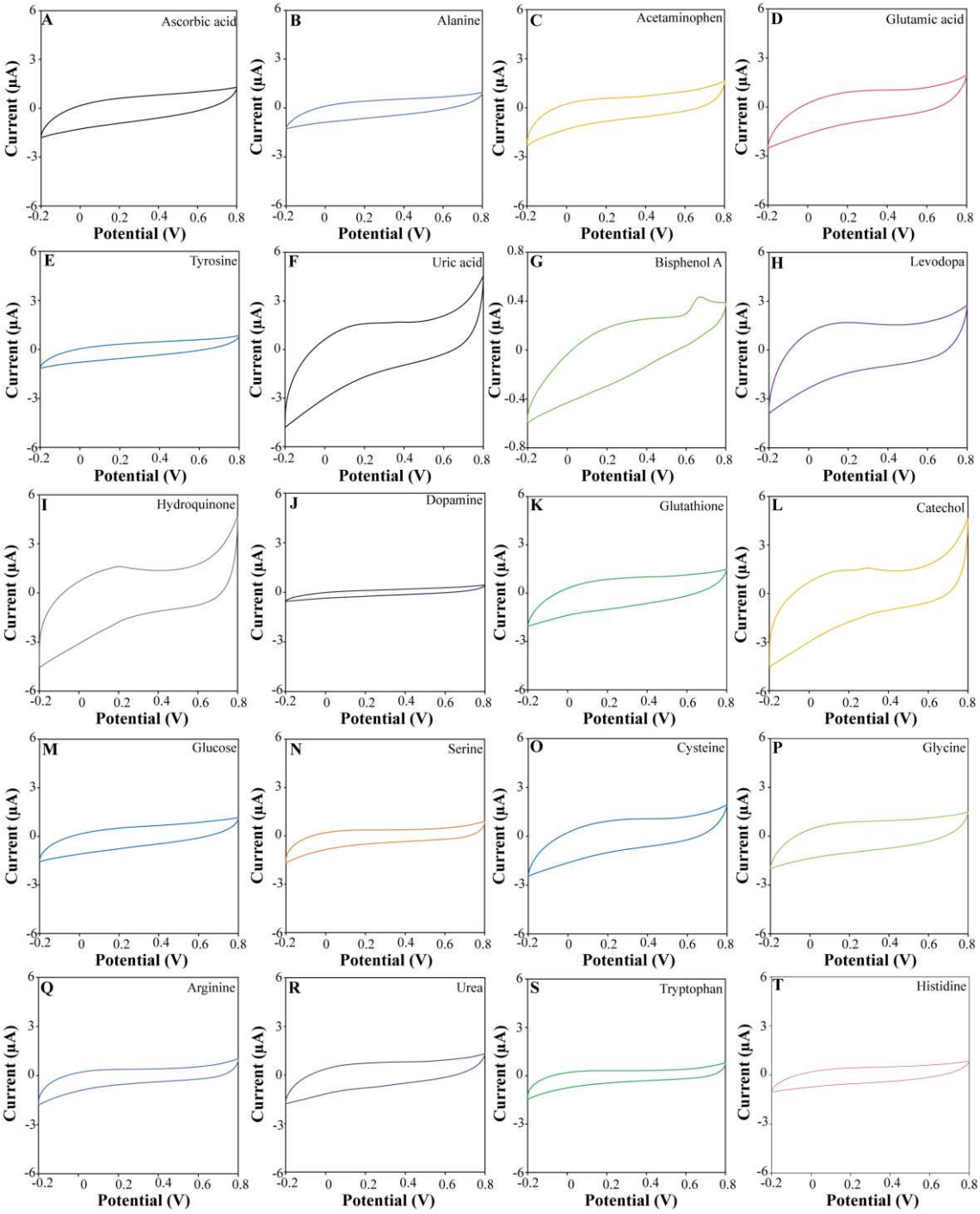


Fig. 6 CV curves of Au-Nb_2O_5/HDBP-GQD electrode in the 1μM of ascorbic acid (A), alanine (B), acetaminophen (C), glutamic acid (D), tyrosine (E), uric acid (F), bisphenol A (G), levodopa (H), hydroquinone (I), dopamine (J), glutathione (K), catechol (L), glucose (M), serine (N), cysteine (O), glycine (P), arginine (Q), urea (R), tryptophan (S) and histidine (T) in the PBS of pH 7.4. The scan rate: 10 mV s^{-1}

A component-omission control was designed to assess the individual roles of Au and HDBP-GQD

in catalytic selectivity. Nb_2O_5 alone was used in place of Au–Nb_2O_5/HDBP-GQD, with identical measurement conditions and analytes as in **Fig. 6**. CV data are shown in **Fig. S2**, and DPV curves for analytes that gave well-defined CV peaks are collected in **Fig. 7**. Fig. 7A and 7B present the DPV responses of Au–Nb_2O_5/HDBP-GQD and Nb_2O_5, respectively.

The Nb_2O_5 electrode behaved distinctly from Au–Nb_2O_5/HDBP-GQD. On Nb_2O_5, acetaminophen, dopamine, bisphenol A, catechol, and hydroquinone all produced clear redox peaks. This indicates broad electrocatalytic activity. Nb_2O_5 can promote electron transfer for various phenolic and amine species. However, it lacks structural discrimination. If selectivity were governed solely by Nb_2O_5, the electrode would respond to many oxidizable analytes. Selective recognition of a target molecule would then be difficult.

Au–Nb_2O_5/HDBP-GQD, in contrast, displayed markedly different DPV features. Peak number, position, current, and shape all changed. These changes suggest that Au and HDBP-GQD do more than improve conductivity. They reshape the recognition and catalytic microenvironment at the electrode/electrolyte interface. Au enhances interfacial electron transfer and lowers the redox overpotential. HDBP-GQD offers recognition sites through its π-conjugated framework and oxygen/nitrogen functional groups. These sites may support π–π stacking, hydrogen bonding, electrostatic interactions, and size/conformation matching. Nb_2O_5 provides metal-oxide redox catalytic centers. Together, these components regulate adsorption orientation, local concentration, proton/electron transfer pathways, and activation energy. Target signals are thus amplified, while non-target redox processes are suppressed. The DPV curve of Au–Nb_2O_5/HDBP-GQD is therefore not a simple sum of the five analytes. It reflects a selective response pattern.

This control provides reverse evidence. When Au and HDBP-GQD are removed, Nb_2O_5 gives obvious CV and DPV peaks for acetaminophen, dopamine, bisphenol A, catechol, and hydroquinone. Thus, Nb_2O_5 alone does not reproduce the catalytic selectivity observed here. Au–Nb_2O_5/HDBP-GQD, by contrast, exhibits markedly different voltammetric behavior. The improved selectivity can

be attributed to the interfacial microenvironment constructed jointly by Au and HDBP-GQD, rather than to Nb_2O_5 itself. This component-omission design helps decouple each component's contribution to selectivity. It also highlights the originality of this work in resolving structure–activity relationships in multicomponent electrocatalysts.

Fig. S2 and **Fig. 7** show that Au and HDBP-GQD markedly reshape the catalytic selectivity of Nb_2O_5-based electrodes. The electrode shifts from broad responses to multiple analytes to differentiated, selective responses. These findings confirm the essential roles of Au and HDBP-GQD in selectivity control. They also provide a direct basis for designing highly selective electrochemical sensing interfaces.

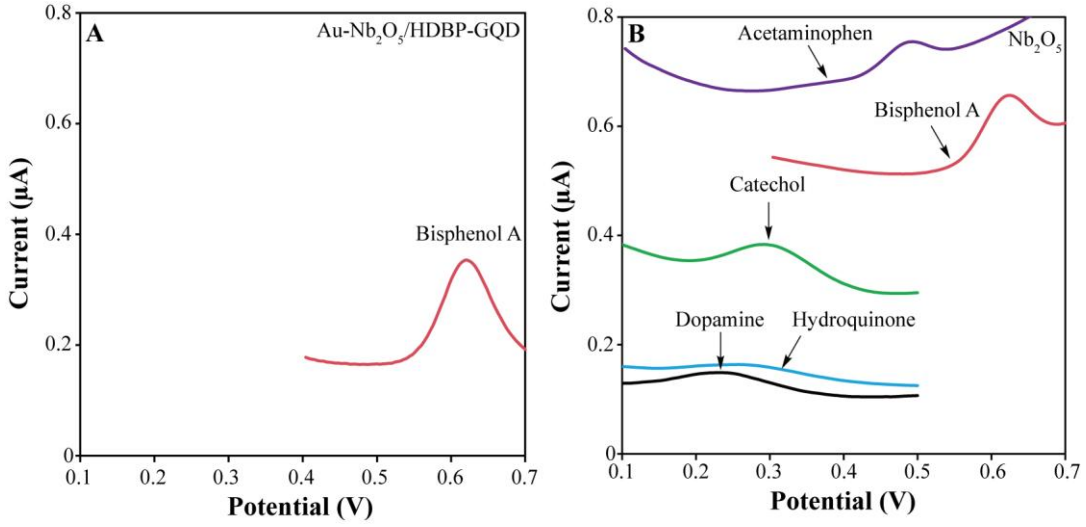


Fig. 7 DPV curves of Au-Nb_2O_5/HDBP-GQD (A) and Nb_2O_5 electrodes (B) in a PBS of pH 7.4 in the presence of 1 μM bisphenol A, acetaminophen, catechol, dopamine and hydroquinone

3.4. Band-Structure Elucidation

To rationalize the superior electrocatalytic selectivity of Au–Nb_2O_5/HDBP-GQD toward bisphenol A (BPA), the semiconductor properties of Nb_2O_5 and Au–Nb_2O_5/HDBP-GQD were examined through optical bandgap, flat-band potential, and band alignment. Tauc plots (**Fig. 8A**) show that Nb_2O_5 has a bandgap of 3.18 eV, characteristic of a wide-bandgap oxide. After introducing Au and HDBP-GQD, the bandgap decreases to 1.835 eV. This narrowing suggests that new electronic coupling channels

form at the composite interface, enhancing visible-light absorption and interfacial charge transfer. Mott–Schottky plots (**Fig. 8B**) exhibit positive slopes, confirming that both materials retain n-type semiconducting behavior. However, the flat-band potential shifts negatively from −0.731 V for Nb_2O_5 to −0.805 V for Au–Nb_2O_5/HDBP-GQD (*vs*. Ag/AgCl). This cathodic shift indicates an upward movement of the conduction band edge and a rise in the Fermi level, reflecting reconstruction of interfacial electron density and band bending. **Fig. 8C** further provides the complete band alignment: Nb_2O_5 has E_{CB} = −0.731 V and E_{VB} = 2.449 V, whereas Au–Nb_2O_5/HDBP-GQD has E_{CB} = −0.805 V and E_{VB} = 1.03 V, with a bandgap of 1.835 eV. The HOMO level of BPA lies at approximately 0.6 V. These results demonstrate that Au and HDBP-GQD are not merely surface modifiers. Instead, they cooperatively regulate the conduction band, valence band, and Fermi level of Nb_2O_5 through band engineering, creating an interfacial electronic structure distinct from that of pristine Nb_2O_5.

This reconstructed energy-level landscape provides a coherent explanation for the enhanced catalytic selectivity of Au–Nb_2O_5/HDBP-GQD. The valence band of Nb_2O_5 is as high as 2.449 V, giving its holes excessive oxidizing power. Such holes can drive electron transfer from various phenolic and amine substrates, leading to broad responses in CV and DPV and poor selectivity. In Au–Nb_2O_5/HDBP-GQD, the valence band shifts to 1.03 V. This value remains positive relative to the BPA HOMO of about 0.4 V, so the thermodynamic driving force for BPA oxidation is preserved. At the same time, the oxidizing power is moderately lowered, creating an energy-level filtering window. Non-target substrates with mismatched HOMO levels can hardly undergo efficient hole transfer. Concurrently, the narrowed bandgap, the raised conduction band and Fermi level, the high conductivity of Au, and the π-conjugated framework and recognition sites of HDBP-GQD work together. These features promote preferential adsorption of BPA at the electrode surface and accelerate interfacial electron transfer, amplifying the target oxidation signal while suppressing non-target oxidation. In this way, band engineering is coupled with molecular recognition. The broad catalysis of Nb_2O_5 is thereby converted into energy-gated selective catalysis, offering a new design

principle for highly selective semiconductor electrocatalytic interfaces.

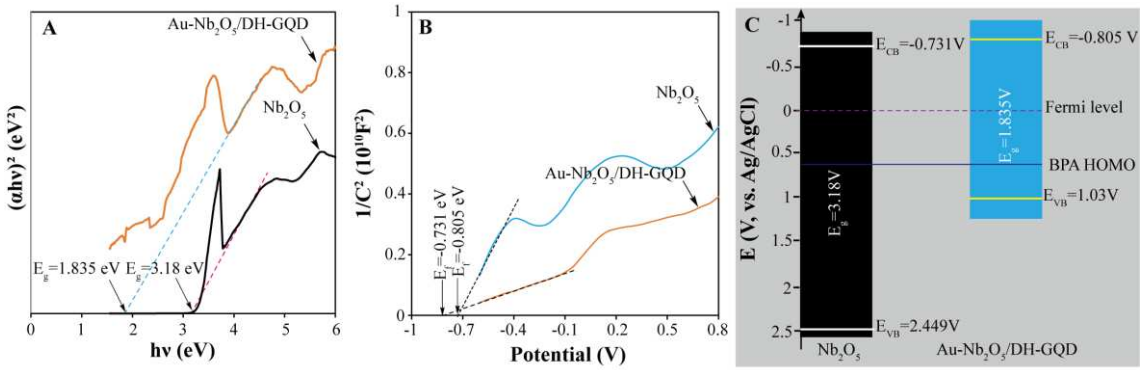


Fig. 8 Band structure characterization of Nb_2O_5 and Au-Nb_2O_5/DH-GQD: Tauc plots (A), Mott–Schottky plots (B) and schematic of band alignment and energy-level matching for BPA oxidation (C)

3.5. Electrochemical detection of bisphenol A

Fig. 9A and **Fig. 9B** jointly establish the feasibility and signal window for BPA electroanalysis. In **Fig. 9A**, cyclic voltammetry (CV) was recorded from −0.2 to 0.8 V, with current plotted in nA. With 100 μM BPA present, a distinct oxidation peak appeared at 0.6 V. **Fig. 9B** narrowed the potential range to 0.4–0.8 V. Under the same BPA concentration, the 0.6 V peak reached 457.2 nA. In the absence of BPA, no discernible peak emerged, and the current remained close to zero. The same peak potential in both windows identifies the 0.6 V response as the intrinsic BPA oxidation signal, rather than a background or window-edge artifact. The near-zero blank current and the 457.2 nA target current together indicate a high signal-to-background contrast. Mechanistically, the phenolic hydroxyl group of BPA undergoes proton-coupled electron transfer near 0.6 V, producing a measurable oxidation current. The blank lacks such redox-active species, so no corresponding peak is observed. Given this CV validation, differential pulse voltammetry (DPV) was selected for BPA quantification. DPV suppresses charging current through differential pulse sampling and enhances the faradaic response. It also offers improved sensitivity and selectivity in complex matrices. DPV was therefore adopted as the electrochemical technique for BPA determination.

Fig. 9C tracks the DPV peak current for 60 μM BPA against the Au-Nb_2O_5/HDBP-GQD volume. The curve is biphasic. At low volumes, the current rises steeply. Added modifier supplies fresh active sites and expands the electroactive area. Interfacial BPA enrichment also intensifies. Together, these effects shorten the electron-transfer path and amplify the faradaic response. The current peaks at 7 μL. At this loading, a continuous conductive network of optimal thickness is likely established. Active sites remain reachable, and BPA diffusion is not yet rate-limiting. Beyond 7 μL, the current plateaus. Excess material thickens the film and promotes stacking or aggregation. Inner active sites become buried, diffusion paths lengthen, and ohmic and capacitive contributions increase. The response thus shifts from site-limited to transport-limited control. The plateau does not reflect a loss of intrinsic catalytic activity; it reflects a growing transport penalty. Therefore, 7 μL defines the balance between active-site density and mass-transport efficiency. This saturation profile identifies the optimal modifier loading for BPA sensing.

Fig. 9D and **9E** show DPV responses of 60 μM BPA in the PBS from pH 4 to 11. The peak current follows a volcano-shaped profile. It is lowest at pH 4, rises sharply from pH 5 to 7, reaches a maximum of about 480 nA at pH 7, stays on a plateau at pH 9–10, and falls at pH 11. The peak potential shifts negatively as pH increases. Each point is the mean of five measurements with SD. This trend arises from three coupled factors: the protonation state of BPA, the surface charge of Au-Nb_2O_5/HDBP-GQD, and the interfacial fate of the oxidation product. At low pH, the phenolic hydroxyl is largely protonated, which raises the barrier for proton-coupled electron transfer (PCET). The modifier is also protonated, weakening π–π stacking and hydrogen bonding with BPA. Both effects lower the current. At pH 7–8, BPA is partially deprotonated, PCET accelerates, and the surface charge matches BPA, improving enrichment and active-site accessibility. The current therefore peaks. At pH 9–11, fully deprotonated BPA oxidizes to phenoxy radicals that readily couple into insulating oligomers. These oligomers coat the electrode and block pores. OH^- competition may also cause modifier aggregation or desorption. The current drop is thus not thermodynamically driven. It reflects

product passivation and mass-transport limitation. The negative peak-potential shift confirms proton involvement in the oxidation step; deprotonation is thermodynamically favorable. Yet the current falls under strongly alkaline conditions. This decouples thermodynamic favorability from kinetic and interfacial constraints. The process shifts from PCET control to product desorption/mass-transport control. pH 7.4 balances PCET rate, enrichment efficiency, and antifouling ability. It was therefore selected as the optimal acidity for BPA determination.

Fig. 9F shows DPV curves for BPA concentrations from 0 to 150 μM. The peak current increases steadily with concentration. **Fig. 9G** plots the peak current against BPA concentration. A linear response is obtained from 0.01 to 150 μM. The regression equation is I_p (nA) = 7.1396 C (μM) + 0.9146, with R^2 = 0.996. The slope of 7.1396 nA μM^{-1} reflects high sensitivity. The limit of detection was determined by substituting three times the standard deviation of ten blank measurements into the calibration equation. This yielded 0.0041 μM. This LOD is notably low, which is significantly lower than that of currently reported methods in **Table 1**. The linear range spans more than four orders of magnitude. Such a wide range is uncommon for BPA sensors. It suggests that the Au-Nb_2O_5/HDBP-GQD interface accumulates BPA without saturation. The abundant active sites and large surface area of the modifier provide a high binding capacity. The HDBP-GQD component may also facilitate fast mass transport through its porous or molecularly imprinted structure. The near-unity R^2 and small intercept indicate that a single dominant mechanism governs the response. This mechanism is likely proton-coupled electron transfer coupled with interfacial enrichment. The low LOD arises from the low background current and the electrocatalytic amplification by Au-Nb_2O_5. The wide linear range allows quantification of both trace and high-level BPA without dilution. This feature is advantageous for real-sample analysis. Overall, the sensor achieves a rare combination of low LOD, high sensitivity, and broad linear range.

Fig. 9H evaluates electrode-to-electrode reproducibility using seven independently prepared Au-Nb_2O_5/HDBP-GQD electrodes. In 65 μM BPA, their DPV peak currents all fall within a narrow

window of about 460–480nA. The bar-to-bar variation is comparable to the error bars. No electrode deviates abnormally. This distribution indicates that the peak current does not depend on accidental features of a single electrode. If Au nanoparticles or Nb_2O_5 aggregated uncontrollably, or if the enrichment capacity of HDBP-GQD fluctuated between batches, the currents would scatter widely. The narrow spread instead suggests that drop-casting produces a continuous and reproducible conductive network. Au nanoparticles supply electron-transfer pathways. Nb_2O_5 provides catalytic oxidation sites. HDBP-GQD creates a BPA-enriching microenvironment. These three functions act in concert across different electrodes. Consequently, the seven electrodes differ little in effective area, interfacial resistance, and BPA adsorption capacity. The signal amplification is dominated by intrinsic catalysis of the material, not by random hot spots or local defects. From a practical standpoint, good electrode-to-electrode reproducibility makes the calibration curve transferable across electrodes. Reliable quantification can be achieved without calibrating each electrode individually. This provides a credible baseline for subsequent storage stability, repeated measurements, and interference tests. **Fig. 9H** thus demonstrates that the sensor meets practical analytical requirements in terms of fabrication reproducibility.

Fig. 9I tracks the DPV peak current of the Au-Nb_2O_5/HDBP-GQD electrode toward 70 μM BPA over seven weeks of storage. The current stays near 500 nA throughout. No variation is smaller than the measurement uncertainty itself. This behavior is consistent with long-term storage stability. The stability likely arises from firm anchoring of the modifier to the electrode. The Au-Nb_2O_5/HDBP-GQD composite may bind through strong adsorption or chemical linkage, so it resists detachment. The Nb_2O_5 crystal structure and the Au nanoparticle conductive network remain intact during storage. The enrichment cavities of HDBP-GQD do not collapse or clog appreciably. Active sites do not aggregate, and interfacial resistance does not rise. BPA enrichment and proton-coupled electron transfer therefore remain efficient after seven weeks. Practically, this storage stability allows electrodes to be prepared in advance and kept for later use. It reduces the fabrication burden for on-

site testing and improves batch-to-batch comparability. Together with **Fig. 9H**, **Fig. 9I** shows that the sensor meets practical analytical requirements in both reproducibility and stability.

Fig. 9J displays the DPV peak current for 70 μM BPA over successive repeated measurements. The current remains essentially constant across the tested cycles. Each data point represents the mean of five replicates, and the error bars overlap substantially. This overlap confirms that cycle-to-cycle variation is minimal. The relative standard deviation stays low, indicating good repeatability. The stable signal suggests that the electrode surface does not foul during repeated scans. The Au-Nb_2O_5/HDBP-GQD layer likely resists accumulation of insulating BPA oxidation products. Its porous architecture may allow soluble oligomers to diffuse away from the interface. Active sites remain accessible, and electron-transfer pathways are preserved. Proton-coupled electron transfer therefore continues efficiently. The sensor can thus be reused multiple times without recalibration. This repeatability is critical for practical deployment. It complements the electrode-to-electrode reproducibility shown in Fig. 9H and the storage stability in Fig. 9I. Together, these results establish the reliability of the sensor for routine BPA analysis.

Fig. 9K assesses the selectivity of the Au-Nb_2O_5/HDBP-GQD electrode by recording DPV peak currents for 70 μM BPA in the presence of various interferents, including inorganic ions (K^+, Na^+, Ca^{2+}, Mg^{2+}, Fe^{3+}, Cu^{2+}, Zn^{2+}, Cl^-, PO_4^{3-}, SO_4^{2-}), small organic molecules, including ascorbic acid (AA), tryptophan, tyrosine, melamine, salicylic acid (SA), tannic acid (TA), benzophenone (BP), caprolactam, thiourea), plastic additives, including 2,6-di-tert-butyl-p-cresol (DTBC), 4-nitrobenzoic acid (NBA), tetraethylthiuram disulfide (TETDS), potassium hydrogen phthalate (PHP), and a surfactant (hexadecyltrimethylammonium bromide, CTAB). Each interferent yields a peak current near the blank (~20 nA), whereas BPA alone produces ~500 nA, a 25-fold difference that confirms strong molecular discrimination. This selectivity likely arises from the combined action of HDBP-GQD enrichment cavities, π–π stacking with the aromatic ring of BPA, and Au/Nb_2O_5 catalytic sites that promote proton-coupled electron transfer only for the correct phenolic substrate; inorganic ions

lack redox activity near 0.6 V, and other organics either oxidize at different potentials or fail to accumulate at the interface.

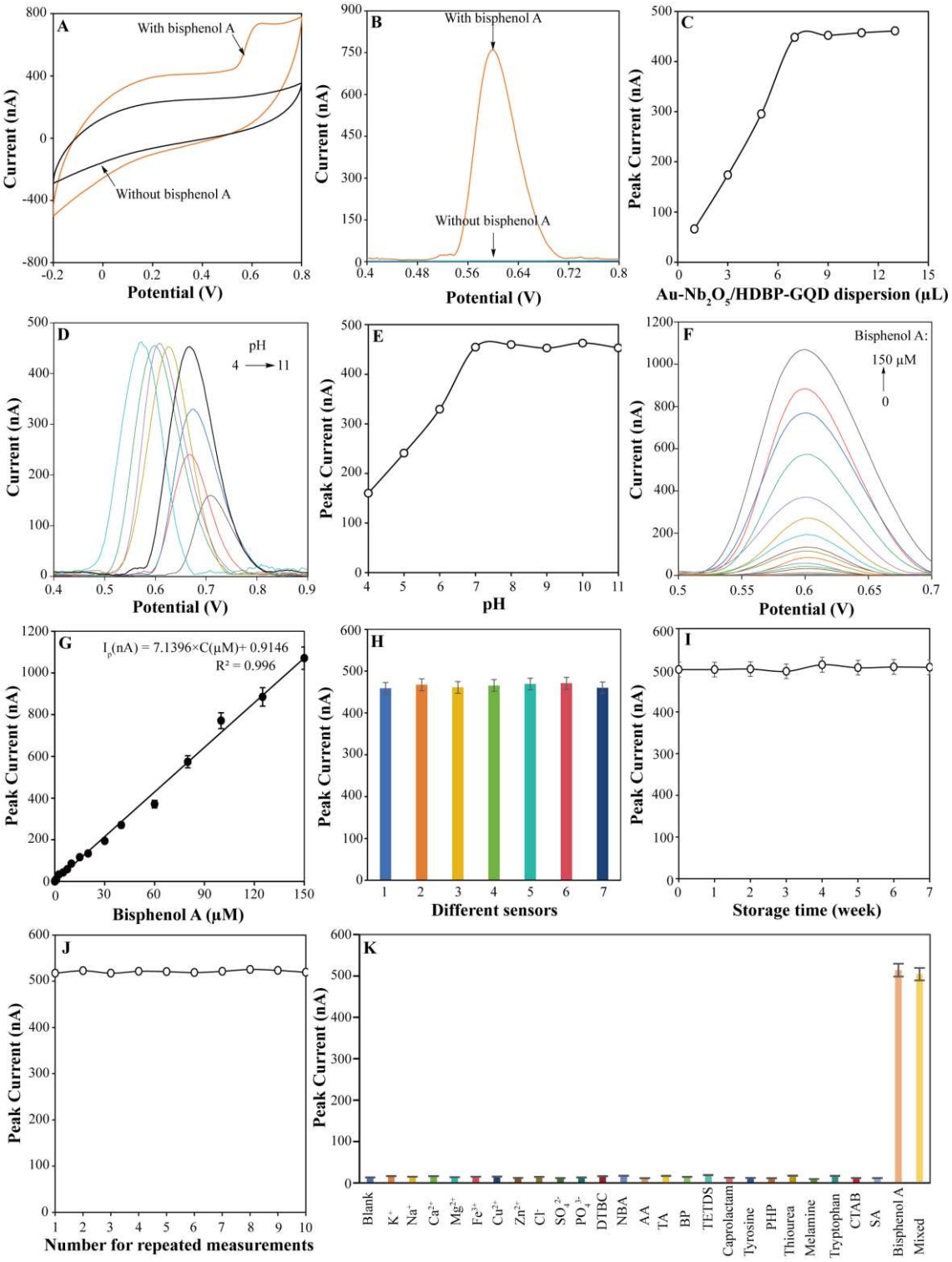


Fig. 9 CV (A) and DPV (B) curves recorded in the absence and presence of 100 μM BPA. Plot of DPV peak current obtained in the presence of 60 μM BPA (C). DPV curves recorded in PBS at pH 4, 5, 6, 7, 8, 9, 10, and 11 in the

presence of 60 μM BPA (D). Plot of DPV peak current versus pH (E). DPV curves recorded at BPA concentrations of 0, 0.01, 0.1, 0.25, 0.5, 0.75, 1, 2.5, 5, 7.5, 10, 15, 20, 30, 40, 60, 80, 100, 125, and 150 μM (F). Corresponding plots of DPV peak current versus BPA concentration (G). DPV peak currents obtained for 65 μM BPA using different sensors (H). Plot of DPV peak current recorded in the presence of 70 μM BPA (I). Plot of DPV peak current for 70 μM BPA as a function of the number of repeated measurements (J). DPV peak currents recorded in the presence of 70 μM interfering species (K). Each data point represents the mean ± SD of five replicate measurements (n = 5).

Table 1 Analytical characteristics of different electrochemical methods for detection of BPA

Materials	Detection Technique	Linear Range (μM)	LOD (μM)	Sample	Ref.
Bimetallic cerium-zinc metal-organic framework/multiwall carbon nanotubes	DPV	0.1–100	0.0072	Packaged drinking water	[36]
Chitosan/gold nanoparticles functionalized with poly[2-(3-thienyl)ethyloxy- 4-butyl-sulfonate] sodium salt	DPV	0.4–20	0.32	Tap water	[37]
Carbon black/functional carbon nanofibers	DPV	0.4–50	0.059	Canned yellow peach, canned dace with black bean, and packaged milk	[38]
Vertically ordered mesoporous silica-nanochannel film	DPV	0.05–1 1.0–10.0	0.015	Pond water, lake water, and soil leaching solution	[39]
Covalent organic framework LZU1/silver nanoparticles	DPV	0.5–100	0.15	Mineral water, electrolyte drink, tea, juice, and beer	[40]
Cobalt-ruthenium-based heterometallic supramolecular polymer	DPV	0.197-2.94 3.5–17.72	0.02	Tap water	[41]
Gold nanoparticle-modified molecularly imprinted polymer	DPV	1.5–7.5	0.161	Drinking water	[42]
Cadmium/reduced graphene oxide composite	DPV	5–110	0.041	River water, tap water, and mineral water	[43]
Bimetallic iron-copper 1,3,5- benzene-tricarboxylic acid metal-organic framework combined with gold nanoparticles	DPV	0.1–1.0 1.0–18	0.018	Rain coat extract	[44]
Single-walled carbon nanotube	LSV	0.5–10	1.0	Tap water and bottled water	[45]

		25–100			
Copper-organic framework/cetyltrimethyl ammonium bromide/graphene composite	DPV	0.1–10 25–800	0.035	Plastic water bottles (PET and PP)	[46]
Palladium-copper bimetallic aerogel	DPV	0.04–85 85–305	0.02	Domestic wastewater, tap water, bottled water, and commercial hair dye	[47]
Triethylenetetramine functionalized multi-walled carbon nanotubes	SWV	1.0–30	0.35	Drinking water, milk, cola, and juice	[48]
Copper, zirconium-1,3,5- benzene tricarboxylate metal-organic framework/carbon nanotube	DPV	2–50	0.5	Tap water	[49]
Au-Nb_2O_5/HDBP-GQD	DPV	0.01-150	0.0031	Plastic bibs, pacifiers, teethers and baby bottle	This work

Saliva was chosen as the extraction medium to better approximate the real-world use of infant-care products and the resulting exposure to BPA. Because saliva contains endogenous species, its matrix effect could matter most at trace BPA concentrations. We therefore examined saliva blanks using DPV. The blank peak current was nearly zero and closely matched that of a pH 7.4 PBS blank. This indicates that saliva itself gave no clear electrochemical response under the chosen conditions and that none of its components produced a detectable electrode signal. We then conducted spike-and-recovery tests in saliva at 0.5, 1.0, and 2.0 μM BPA. The recoveries were 99.08%, 100.20%, and 100.17%, respectively. Together, the near-zero blank response and consistent recoveries show that saliva does not meaningfully interfere with trace BPA detection. These findings support the method's resistance to matrix effects and its quantitative reliability in a medium that better reflects actual exposure conditions.

3.6. Sample analysis

Infant care products were obtained from major supermarket chains in China and randomly selected from the 0–12 months category, comprising baby bottles, pacifiers, teethers, and plastic bibs. BPA in the migration solution was quantified by electrochemical detection after the pretreatment and migration described above (n = 5). **Table 2** shows no detectable BPA in unspiked samples. Across the

0.5–2.0 μg kg^{-1} spiking range, recoveries were 98.8%–101.9% and RSDs were 1.1%–3.0%. These values support the method's accuracy and precision for BPA analysis in the tested infant care products.

Table 2 The results for electrochemical detection of BPA in infant care products (N=5)

Sample	Spiked BPA (μM)	Found BPA (μM ± SD)	Recovery (%)	RSD (%)
Baby bottle	0	No found		
	0.5	0.49±0.01	98.9	2.8
	1.0	0.99±0.02	99.3	2.1
	2.0	2.01±0.04	100.8	2.1
Pacifiers		No found		
	0.5	0.49±0.01	99.6	3.0
	1.0	0.99±0.02	99.5	2.5
	2.0	1.99±0.06	99.8	2.8
Teethers		No found		
	0.5	0.51±0.01	101.5	2.9
	1.0	1.02±0.03	101.9	2.5
	2.0	1.99±0.02	99.3	1.1
Plastic bibs	0	No found		
	0.5	0.49±0.01	98.8	2.7
	1.0	1±0.02	99.8	2.4
	2.0	1.99±0.04	99.4	2.1

Conclusions

This study establishes an energy-selective electrocatalytic strategy that integrates atomic-level electron coupling with multi-heteroatom interfacial band engineering. Functionalized heteroatom-doped graphene quantum dots serve as chelating and interfacial modifiers, enabling atomic-level Au confinement within the Nb_2O_5 lattice while heteroatom doping tailors the interfacial energy levels. The resulting architecture creates an energy-level-gated electron-transfer pathway, in which the composite energy levels are aligned with the oxidation potential of the target analyte. Such alignment

allows preferential target electrooxidation in complex matrices while suppressing coexisting interferents. This strategy converts the nonselective electron transfer of zero-bandgap materials into energy-selective catalysis, extending the recognition mechanism from molecular recognition to energy-level recognition. The electronic-state engineering approach is general and offers a new design principle for anti-interference detection of trace targets in complex systems. It is expected to promote multi-target sensing and electrocatalysis in food safety, environmental monitoring, and clinical diagnostics.

Acknowledgements

The authors acknowledge the Chemical Testing Center of the School of Chemistry and Materials Engineering, Jiangnan University for support.

Funding

This work was supported by The National Key Research and Development Program of China (No. 2021YFA0910200).

Ethics approval and consent to participate

Not applicable. All experiments were conducted on sweat samples, which, according to the institutional policies of Jiangnan University, do not qualify as clinical specimens. Consequently, ethical committee approval and participant informed consent were not required for this study.

Clinical trial number

Not applicable. This study does not meet the definition of a clinical trial, as it involves only non-clinical sweat samples. Accordingly, no clinical trial registration number has been assigned.

Author contributions

Li Xinyan: Investigation. **Li Ruiyi**: Investigation and Conceptualization. **Li Zaijun**: Methodology.

Data availability

Data is provided within the manuscript or supplementary information files.

Competing interests

The authors declare no competing interests.

References

[1] A. Agarwal, S. Gandhi, A.D. Tripathi, A. Gupta, M. Iammarino, J.K. Sidhu, Food contamination from packaging material with special focus on the Bisphenol-A, Crit. Rev. Biotechnol. 45 (2025) 2344571. https://doi.org/10.1080/07388551.2024.2344571

[2] S. Bhardwaj, S. Misra, Systems Toxicology of bisphenol A: mechanistic overlap in metabolic and reproductive disruption, J. Appl. Toxicol. 46 (2026) 1779–1800. https://doi.org/10.1002/jat.70127

[3] M. Caglayan, S. Ozden, Potential impacts of bisphenols on prostate cells: An overview of cytotoxicity, proliferation, oxidative stress, apoptosis, and ER-stress response activation, Food Chem. Toxicol. 184 (2024) 114416. https://doi.org/10.1016/j.fct.2023.114416

[4] R.S. Kaulgud, S. Belur, A.M. Anagharani, S. Veeresh, A.K. Shettar, Effects of Bisphenol-A on human endocrine function and health outcomes: a review, Discov. Toxicol. 2 (2025) 24 https://doi.org/10.1007/s44339-025-00046-6

[5] I. Neri, G. Russo, L. Grumetto, Bisphenol A and its analogues: from their occurrence in foodstuffs marketed in Europe to improved monitoring strategies-a review of published literature from 2018 to 2023, Arch. Toxicol. 98 (2024) 2441-2461. https://doi.org/10.1007/s00204-024-03793-4

[6] C.E. Pop, B.A. Miu, D. Németh, R. Wolff, D.F. Mihăilescu, S.M. Avramescu, M. Mernea, Bisphenol A analysis and quantification inconsistencies via HPLC-UV: a systematic review with technical notes, Discov. Appl. Sci. 6 (2024) 171. https://doi.org/10.1007/s42452-023-05617-z

[7] J. Ośko, M. Grembecka, Charged Aerosol Detection as a Versatile Tool in Modern Food Analysis: Applications, Detector Comparisons, and Future Perspectives, Appl. Sci. 16 (**2026**) 6904. https://doi.org/10.3390/app16146904

[8] F. Khamidova, U. Tatykayeva, G. Reymnazarova, S. Davronova, I. Tilyabov, S. Khasanov, Mass spectrometry in laboratory medicine: advances in automation, multiplex biomarker quantification, and diagnostics, Clin. Chim. Acta 591 (2026) 121128, https://doi.org/10.1016/j.cca.2026.121128

[9] A. Jbebli, K. Coufalikova, M. Zanaboni, M. Bergna, R. Picenoni, J. Klanova, E.J. Price,

Automated sequential derivatization for gas chromatography-[orbitrap] mass spectrometry-based metabolite profiling of human blood-based samples, Bio. Protocol. 15 (2025) e5196. https://doi.org/10.21769/BioProtoc.5196

[10] K. Patil, S. Upadhye, S. Shetty, Lateral flow immunoassays: challenges and innovations, Clin. Chim. Acta 593 (2027) 121269, https://doi.org/10.1016/j.cca.2026.121269

[11] X. Ma, R. Zhu, H. Zhang, Z. Meng, pH-responsive persistent luminescence nanoprobes biosensor for autofluorescence-free determination of glucose level in human samples and fingerprint encryption, Luminescence. 39 (2024) e4900. https://doi.org/10.1002/bio.4900

[12] M. Eshtiaghi, A.S. Maghsoudi, A. Khodarahmi, B. Ramezanzadeh, F. Pishbin, S. Hassani, Ternary poly(3,4-ethylenedioxythiophene) polystyrene sulfonate/ $Ti_3C_2T_x$/ silver nanowire electrochemical aptasensor for bisphenol A detection, Colloid. Surface. A, 727 (2025) 138416, https://doi.org/10.1016/j.colsurfa.2025.138416

[13] Y. Zhang, Z. Yang, J. Deng, Y. Zhang, H. Li, C. Li, W. Xu, Z. Hou, B. Zhou, CoNi-MOF/PANI/RGO-based molecularly imprinted electrochemical sensor for the detection of bisphenol A, J. Food Compos. Anal. 147 (2025) 108035. https://doi.org/10.1016/j.jfca.2025.108035

[14] D. Zhou, K. Meng, F. Chen, Y. Zhang, L. Ji, X. Hu, X. Li, N. Yang, Portable electrochemical platform integrating MnOOH/expanded graphite composites and smartphone for on-site detection of bisphenol pollutants, Chem. Eng. Sci. 339 (2027) 125114. https://doi.org/10.1016/j.ces.2026.125114

[15] D. Arumugam, M.M. Ahmed, Z. Zeb, Y. Gao, H. Pang, Nanocarbon sensors: Unlocking efficient detection of water pollutants through electrocatalysis, J. Food Compos. Anal. 148 (2025) 108357. https://doi.org/10.1016/j.jfca.2025.108357

[16] K. Jayakumar, V. Veeramuthu, J. Lee, MXene-driven electrochemical platforms for bisphenol A sensing: Surface group interactions and reaction mechanisms, J. Environ. Chem. Eng. 14 (2026)

120676. https://doi.org/10.1016/j.jece.2025.120676

[17] F. Rejab, N.E. Dardouri, A. Rouis, M. Echabaane, H. Nasri, H.B. Halima, N. Jaffrezic-Renault, A Novel Electrochemical Platform Based on Cadmium (II) (fluorophenyl)Porphyrin and Gold Nanoparticles Modified Screen-Printed Electrode Electrode for the Sensitive Detection of Bisphenol A, Electroanalysis. 37 (2025) 12017. https://doi.org/10.1002/elan.12017

[18] C. Zhou, Y. Zhu, Z. Zhao, X. Dong, A. Kushwaha, M. Muddassir, A. Kumar, Y. Pan, Electrochemical sensing of Bisphenol A using bimetallic porphyrin MOFs modulated by different carboxylic acid analogs, Microchem. J. 220 (2026) 116464. https://doi.org/10.1016/j.microc.2025.116464

[19] R. Sasikumar, B. Akila, S.M. Chen, J. Kim, B. Kim, Towards Safer Water: A Low-Cost Disposable Electrochemical Sensor for Bisphenol A Using $La_2Sn_2O_7$ Nanostructures, Glob Chall. 10 (2026) e00579. https://doi.org/10.1002/gch2.202500579

[20] M.E. Corman, A. Cetinkaya, C. Armutcu, E. Bellur Atici, L. Uzun, S.A. Ozkan, A sensitive and selective electrochemical sensor based on molecularly imprinted polymer for the assay of teriflunomide, Talanta 249 (2022) 123689. https://doi.org/10.1016/j.talanta.2022.123689

[21] Y. Jiang, Y. Zhang, L. Wan, C. Cui, P. Guo, D. Han, W. Tan, Structural basis and affinity improvement for an ATP-binding DNA aptamer, Proc. Natl. Acad. Sci. U.S.A. 122 (2025) e2506491122. https://doi.org/10.1073/pnas.2506491122

[22] Y. Zhang, Z. Zhou, Y. Kang, S. Wu, M. Yu, Y. Zhang, L. Qian, Laccase-based electrochemical sensors: A comprehensive review on fabrication, mechanism, and multifaceted applications, TrAC-Trend. Anal. Chem. 200 (2026) 118814. https://doi.org/10.1016/j.trac.2026.118814

[23] S. Sawan, R.-M. Hage, R. Maalouf, MXene–molecularly imprinted polymer electrochemical sensors: A systematic review and meta-analysis, Sensors and Actuators Reports 11 (2026) 100455. https://doi.org/10.1016/j.snr.2026.100455

[24] D. Xu, R.Y. Li, G. Wang, H. Zhu, Z.J. Li, Electrochemical detection of carbendazim in strawberry

based on a ruthenium–graphene quantum dot hybrid with a three-dimensional network structure and Schottky heterojunction, New J. Chem. 45 (2021) 21308–21314. https://doi.org/10.1039/d1nj04602k

[25] C. Rime, S. Delic, A. Onidi, L. Cretegny, N.B. Hopf, D. Staedler, F. Lucarini, Assessing bisphenols migration from children's products on the Swiss market: simulated oral exposure and risk implications, Chemosphere 393 (2025) 144772, https://doi.org/10.1016/j.chemosphere.2025.144772

[26] X.L. Kuang, R.Y. Li, Z.J. Li, Dual engineering of electronic and interfacial structures via erbium doping and graphene quantum dots for high-entropy alloy toward high performance non-enzymatic electrochemical glucose sensing, J. Alloy. Compd. 1074 (2026) 189149. https://doi.org/10.1016/j.jallcom.2026.189149

[27] S. Chen, Y.H. Hu, Rational Design of Catalytically Active Sites in Metal-Free Carbon Materials for Electrocatalytic CO_2 Reduction: A Review, Energy & Fuels 39 (2025) 7649-7664. https://doi.org/10.1021/acs.energyfuels.5c00352

[28] X.S. Li, R.Y. Li, Y.Q. Yang, Z.J. Li, Atomic Ru-embedded three-dimensional ion-conductive tunnel networks in Ta/Ru co-doped Nb_2O_5 nanosheets enabled by multifunctional graphene quantum dots for ultrahigh-energy-density supercapacitors, Appl. Surf. Sci. 708 (2025) 163765. https://doi.org/10.1016/j.apsusc.2025.163765

[29] P. Aniceto-Ocana, J. Marqueses-Rodriguez, J.M. Munoz-Ocana, M.J. Fernandez-Trujillo, A.G. Algarra, A.M. Rodriguez-Chia, J.J. Calvino, C.E. Castillo, M. Lopez-Haro, An AI-Powered Methodology for Atomic-Scale Analysis of Heterogenized Correlated Single-Atom Catalysts, Small Methods. 9 (2025) 2402010. https://doi.org/10.1002/smtd.202402010

[30] S. Sozhaveni, S.J. Jeyakumar, S. Ramalingam, Defect-Engineered Mo-Doped Nb_2O_5 nanoparticles: structural strain modulation, optical bandgap tuning, photoluminescence behavior, and enhanced antibacterial activity, J. Electron. Mater. 55 (2026) 8910-8927. https://doi.org/

10.1007/s11664-026-13090-8

[31] P. Yan, R.Y. Li, Z.J. Li, Molecular-level biomimetic integration of phosphorus-doped graphene quantum dots with silver nanoparticles for highly stable and active nanozymes: Application in ultrasensitive ascorbic acid detection, Spectrochim. Acta A 357 (2026) 127747. https://doi.org/10.1016/j.saa.2026.127747

[32] Q.Q. Zhang, R.Y. Li, Y.Q. Yang, Z.J. Li, Ultrasensitive electrochemical sensor for monitoring uric acid in sweat based on hexagonally-structured $Co_2CrMnFeNi$ high-entropy alloy nanosheets with exceptional catalytic performance, Sensor Actuat. B-Chem. 438 (2025) 137790. https://doi.org/10.1016/j.snb.2025.137790

[33] S.S. Kalanur, I.H. Yoo, I.S. Cho, H. Seo, Niobium incorporated WO_3 nanotriangles: Band edge insights and improved photoelectrochemical water splitting activity, Ceram. Int. 45 (2019) 8157-8165. https://doi.org/10.1016/j.ceramint.2019.01.117

[34] Yue. Pan, R.Y. Li, Z.J. Li, Electrochemical biosensor based on Au_5Ir@graphene quantum dot nanocomposite and DNA walker for detection of atrazine in environmental water with extremely high sensitivity and selectivity, Sensor Actuat. B-Chem. 423 (2025) 136873. https://doi.org/10.1016/j.snb.2024.136873

[35] Y. Yu, S. Wang, Y. Liu, X. Duan, X. Guan, Pulsed Electrolysis Unlocks Non-Noble-Metal Catalysis for Per- and Polyfluoroalkyl Substance Defluorination in Water, J. Am. Chem. Soc. 148 (2026) 37034–37045. https://doi.org/10.1021/jacs.6c10422

[36] D. Huang, X. Huang, J. Chen, R. Ye, Q. Lin, S. Chen, An Electrochemical Bisphenol: a Sensor Based on Bimetallic Ce-Zn-MOF, Electrocatalysis 12 (2021) 456–468. https://doi.org/10.1007/s12678-021-00659-6

[37] L.A. Almeida, B.V.M. Rodrigues, D.T. Balogh, R.C. Sanfelice, L.A. Mercante, A.F. Frade-Barros, A. Pavinatto, Chitosan/Gold Nanoparticles Nanocomposite Film for Bisphenol A Electrochemical Sensing, Electrochem. 3 (2022) 239-247. https://doi.org/10.3390/electrochem3020016

[38] J. Wang, Z. Yang, S. Gu, M. Pan, L. Xu, A Facile Electrode Modification Approach Based on Metal-Free Carbonaceous Carbon Black/Carbon Nanofibers for Electrochemical Sensing of Bisphenol A in Food, Foods 14 (2025) 314. https://doi.org/10.3390/foods14020314

[39] J. Huang, T. Zhang, G. Dong, S. Zhu, F. Yan, J. Liu, Direct and Sensitive Electrochemical Detection of Bisphenol A in Complex Environmental Samples Using a Simple and Convenient Nanochannel-Modified Electrode, Front. Chem. 10 (2022) 900282. https://doi.org/10.3389 /fchem.2022.900282

[40] Y.H. Pang, Y.Y. Wang, X.F. Shen, J.Y. Qiao, Covalent organic framework modified carbon cloth for ratiometric electrochemical sensing of bisphenol A and S, Mikrochim. Acta 189 (2022) 189. https://doi.org/10.1007/s00604-022-05297-3

[41] A. Awal, S. Islam, T. Islam, M.M. Hasan, S.M.A. Nayem, M.M.H. James, M.D. Hossain, A.J.S. Ahammad, Facile Chemical Synthesis of Co-Ru-Based Heterometallic Supramolecular Polymer for Electrochemical Oxidation of Bisphenol A: Kinetics Study at the Electrode/Electrolyte Interface, ACS Omega 8 (2023) 28355–28366. https://doi.org/10.1021/acsomega.3c02206

[42] F. Yilmaz, N.A. Shama, S. Asir, H. Cobanogullari, E. Yolac, A. Kiraz, I. Gokturk, A. Denizli, D. Turkmen, Gold Nanoparticle-Modified Molecularly Imprinted Polymer-Coated Pencil Graphite Electrodes for Electrochemical Detection of Bisphenol A, ACS Omega 10 (2025) 740–753. https://doi.org/10.1021/acsomega.4c07688

[43] M. Nawaz, H. Shaikh, J.A. Buledi, A.R. Solangi, R. Raza, B. Maher, Microwave-assisted synthesis of cadmium/reduced graphene oxide composite: an operative platform for highly specific electrochemical determination of bisphenol-A, J. Appl. Electrochem. 53 (2022) 751–764. https://doi.org/10.1007/s10800-022-01797-5

[44] M.B. Nguyen, N.H. Anh, V. Thi Thu, P. Thi Hai Yen, P. Hong Phong, L. Quoc Hung, N.T.T. Ngan, T.Q. Hai, V. Thi Thu Ha, A novel bimetallic MOFs combined with gold nanoflakes in electrochemical sensor for measuring bisphenol A, RSC Adv. 12 (2022) 33825–33834.

https://doi.org/10.1039/d2ra06300j

[45] C. Bui, G. La Flower, J. Paudyal, Electrochemical sensing of bisphenol A on single-walled carbon nanotube paper electrodes, Electroanalysis 35 (2023) e202200449. https://doi.org/10.1002/elan.202200449

[46] L. Zhang, H. Ma, H. Sun, X. Zhang, R. Sun, H. Zheng, H. Wang, Y. Wang, J. Guo, Y. Liu, Y. Qi, A copper-organic framework/graphene modified electrode for sensitive electrochemical detection of bisphenol A, J. Appl. Electrochem. 55 (2024) 177–188. https://doi.org/10.1007/s10800-024-02160-6

[47] Z. Fang, J. Wang, Y. Xue, M. Khorasani Motlagh, M. Noroozifar, H.B. Kraatz, Palladium-Copper Bimetallic Aerogel as New Modifier for Highly Sensitive Determination of Bisphenol A in Real Samples, Materials (Basel) 16 (2023) 6081. https://doi.org/10.3390/ma16186081

[48] M. Çakıcı, A.A. Avan, H. Filik, E. Kök Yetimoğlu, Individual and Simultaneous Electrochemical Detection of Bisphenol A and Bisphenol S in Food Samples Using Triethylenetetramine Functionalized Multi-Walled Carbon Nanotubes, Food Anal. Method. 16 (2022) 225–237. https://doi.org/10.1007/s12161-022-02409-w

[49] N.N. Tien, N.T. Dat, N.B. Manh, N.D. Hieu, V.C. Tu, N.T.T. Ngan, V.T.T. Ha, P. Decorse, B. Piro, V.T. Thu, Cu,Zr-BTC/CNT composite for electrochemical detection of endocrine disruptor bisphenol A, J. Mater. Sci. 58 (2023)16699–16713. https://doi.org/10.1007/s10853-023-09083-1

Supplementary Files

This is a list of supplementary files associated with this preprint. Click to download.

- Electronicsupportinginformation.docx